



ATLAS NOTE

May 20, 2010



Underlying event particle flow based on calorimeter clusters in pp collisions at 7 TeV with the ATLAS detector at the LHC

C. Bertella^a, S. Chekanov^b, P. Giovaninni^c, N. Kanaya^d, S. Menke^c, J. Proudfoot^b, C. Roda^a,
P. Starovoitov^e, I. Vivarelli^f, R. Yoshida^b, J. Zhang^b

^a*INFN, Pisa, Italy*

^b*Argonne National Laboratory, IL, USA*

^c*Max Plank Institute fur Physik, Munich, Germany*

^d*Tokyo University, Japan*

^e*CERN CH-1211, Geneve 23, Switzerland*

^f*Albert Ludwigs Universitat Freiburg, Germany*

Abstract

Data were collected in 2010 using proton-proton collisions at a center of mass energy of 7 TeV were used to study particle flow correlations. Particle flows are measured in the minimum bias events using clusters of energy in the ATLAS calorimeters, taking advantage of their fine granularity. The results on the angular correlation between clusters and the correlation between the mean cluster momentum and the number of clusters are presented. The results are compared to the 900 GeV results and Monte Carlo predictions.

1 Introduction

The current note extends the underlying event studies presented for 900 GeV data in Ref. [1]. As for the previous note, the current studies use clusters of energy (termed topoclusters in the remainder of this paper). The measurement is performed in three regions of phase space, as shown in Figure 1 where the "transverse" region is the region which is considered to be the most affected by the soft QCD processes responsible for the underlying event.

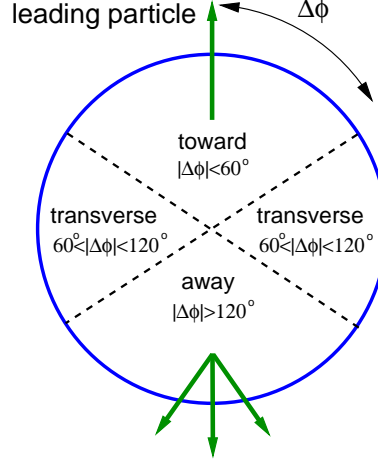


Figure 1: A schematic representation of several phase-space regions used for studies in this note

As explained in [1], the studies using topoclusters have several important features. Firstly, it provides a means to be sensitive to the entire hadronic final state (including neutral hadrons). Secondly, the analysis is complementary to the corresponding analysis using charged particles but with completely independent systematics. Finally, jet reconstruction is based almost entirely on energy deposition in the calorimeter and this analysis of the underlying event can be used directly to estimate the effect of underlying event on the jet energy measurement.

2 Data selection and MC samples

The data used in this analysis were taken in 2010 during which period the LHC operated at a center of mass energy of 7 TeV. The calorimeter systems were essentially fully functional; during this running period, there were approximately 2% non-functional channels in the tile hadronic calorimeter and approximately 1% non-functional channels in the liquid argon calorimeters [2, 3].

The 7 TeV data used in this analysis were collected during 2010. The following runs were used: 152166 (206 ≤ *lbn* ≤ 300), 152221 (5 ≤ *lbn* ≤ 167), 152214 (159 ≤ *lbn* ≤ 201) 152345 (128 ≤ *lbn* ≤ 207), 152409 (124 ≤ *lbn* ≤ 716), 152441 (307 ≤ *lbn* ≤ 672), 152777 (58 ≤ *lbn* ≤ 339), 152844 (177 ≤ *lbn* ≤ 234). This corresponds to an integrated luminosity of about 238 μb⁻¹. A total of about 7.7M events were collected from colliding proton bunches in which the MBTS_1 trigger recorded one or more hits on either side of the calorimeter.

The events to be analyzed were selected using an identical procedure as described in [4]. In a similar approach to that presented in [4], only clusters with $p_T > 0.5$ GeV and $|\eta| < 2.5$ ¹ are considered. The datasets used were those obtained from the first reprocessing. The analysis was done using

¹ E_T > and p_T are respectively the cluster energy and momentum transverse to the beam direction.

ESD/AOD files, converting them into the NtupleMaker [5] format to reduce the size and to increase the data reading rate. The NtupleMaker keeps information on topoclusters and truth particles in the form of a TLorentzVector-derived class (unlike D3PD which are based on vectors of numbers).

The QCD predictions for the hadronic final state in pp collisions are based on the PYTHIA 6.4 Monte Carlo model [6]. This model is based on the MC09 tune [7] which employs the p_T -ordered parton shower and the MRST LO* parton density functions [8]. The parameters were adjusted to describe charged-multiplicity distributions in minimum-bias events measured at 630 GeV and 1.8 TeV in $p\bar{p}$ collisions [9].

In addition to the MC09 tune, the following two PYTHIA parameter sets are used: (1) the Perugia0 set [10] in which the soft-QCD part is tuned using only minimum-bias data from the Tevatron and CERN $p\bar{p}$ colliders; (2) the DW[11] PYTHIA tune, which uses the virtuality-ordered showers and was derived to describe the CDF Run II underlying event and Drell-Yan data.

The following Monte Carlo data sets were used at the AOD level:

```
mc09_7TeV.105001.pythia_minbias.recon.AOD.e517_s764_s767_r1204
mc09_7TeV.108313.pythia_minbias_Perugia0.recon.AOD.e514_s764_s767_r1204
mc09_7TeV.108310.pythia_minbias_DW.recon.AOD.e514_s764_s767_r1204
mc09_7TeV.106096.PhofjetNdiff.recon.AOD.e514_s764_s767_r1204
mc09_7TeV.106097.PhofjetSdiff.recon.AOD.e514_s764_s767_r1204
mc09_7TeV.106098.PhofjetDdiff.recon.AOD.e514_s764_s767_r1204
```

The main analysis is done with the first MC set, while the other two tunes are used for systematics studies as discussed below. The PHOJET MC model [12] was used to check the diffractive contribution as discussed in Sect. 6.

For the corrections, the truth particles are selected if their lifetimes τ are smaller than $3 \cdot 10^{-10}$ seconds. Neutrinos are excluded from consideration. According to this definition, K_0^S 's, Λ 's and Σ^\pm are treated as stable particles particle².

To provide high statistics Monte Carlo samples for comparison with the unfolded data and in order to study other MC tunes, the NtupleMakerTruth [13] was used to generate ROOT tree with TLorentzVector records. The official Monte Carlo production option files were used. The truth level to be shown on all final figures was generated with the statistics a factor 5-10 larger than that used for data unfolding.

3 Analysis Strategy

This note extends Ref. [1] with similar studies using the 900 GeV data.

Figure 2 shows the number of reconstructed topoclusters versus the number of stable particles in simulated minimum bias events. Reconstructed topoclusters are required to have $p_T > 0.5$ GeV. The figure shows strong correlation and it is clearly meaningful to consider topoclusters a measure of particle activity.

Similarly, Figure 3 shows the correlation between the calibrated topoclusters and the primary tracks selected as discussed in the track-based studies [14, 15]. A perfect correlation is observed for data and the Monte Carlo simulation. The average and the RMS values of this 2D distribution agree with the MC simulation within a few %. The Kolmogorov-Smirnov (KS) test reports that the data and MC distributions are approximately identical (with a probability of 9.9999999942936424e-01).

The analysis presented here follows a similar approach to that which has been carried using only charged particles [14, 15]. We will first show that the topocluster distributions in pp collisions are well modeled in full simulation. A key issue and one which is critical in determining topocluster multiplicity

²For the AOD/ESD analysis, all particles with the barcode above 200000 or equal 0 were removed.

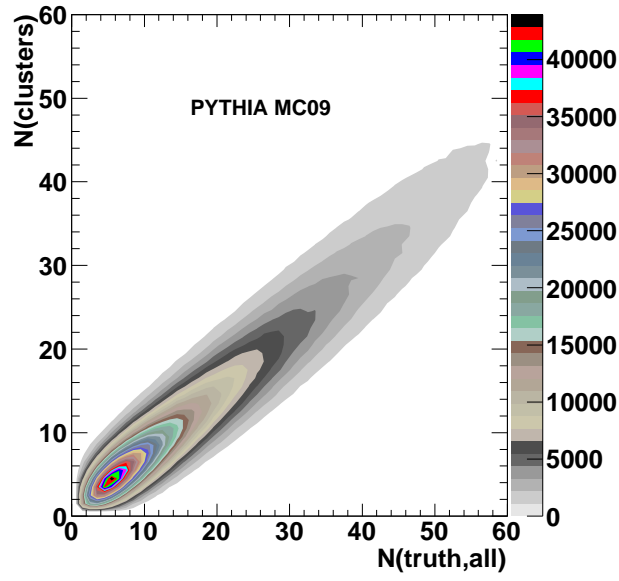


Figure 2: Correlation between multiplicities of calibrated topocluster and stable truth particles in PYTHIA MinBias events at a centre of mass energy of 900 GeV.

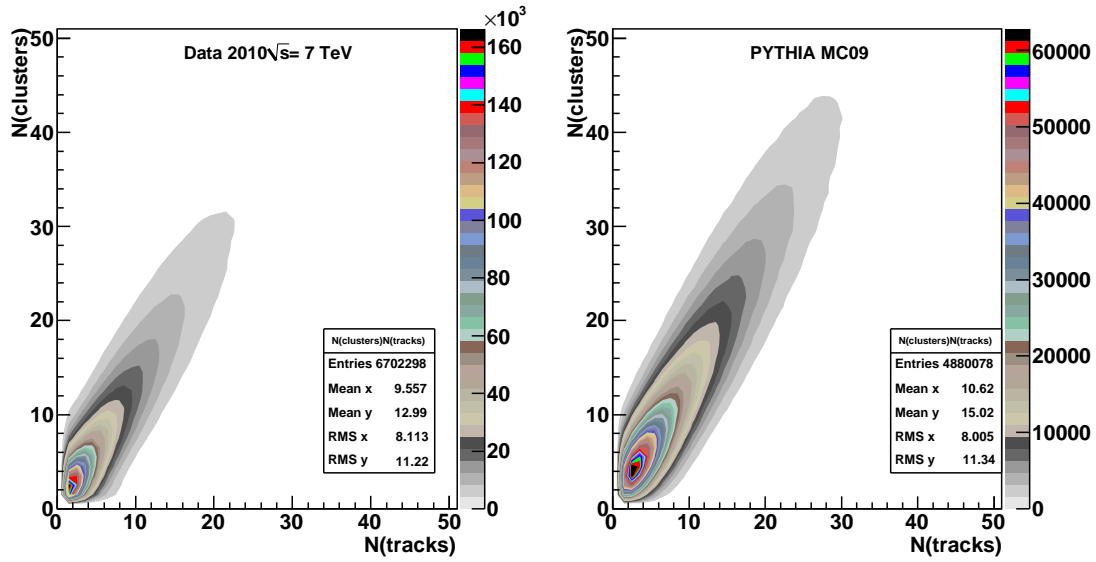


Figure 3: Correlation between multiplicities of calibrated topocluster and primary tracks in data and PYTHIA MinBias events at a centre of mass energy of 900 GeV.

is the calorimeter energy scale and its modeling in the ATLAS simulation. This is established using the response of the calorimeters for isolated charged hadrons as a function of particle momentum and also checked using π^0 decays reconstructed using standard topoclusters. Finally, the large variation in response as a function of particle momentum introduces a variation in acceptance and the Monte Carlo is used to determine bin-by-bin correction factors to correct observed distributions to stable particle distributions. These may then be used for comparison to model predictions for minimum-bias events.

4 Topocluster properties

Figure 4 shows a comparison between pp collision data and the minimum bias MC simulation for several topocluster variables, selecting the topoclusters with $p_T > 0.5$ GeV: the number of clusters, the p_T , η and ϕ distributions, where the distributions are normalized to unit area. The Monte Carlo includes all known detector inefficiencies such as those from non-functional calorimeter channels as well as our best knowledge of the material in front of the calorimeter (such as from the inner detector and its services). Excellent agreement is observed for PYTHIA MC09 and PYTHIA Perugia0 tune for p_T , η and ϕ . Small discrepancies between data and Monte Carlo are seen for the multiplicity distribution which are attributed to the presence of diffractive events.

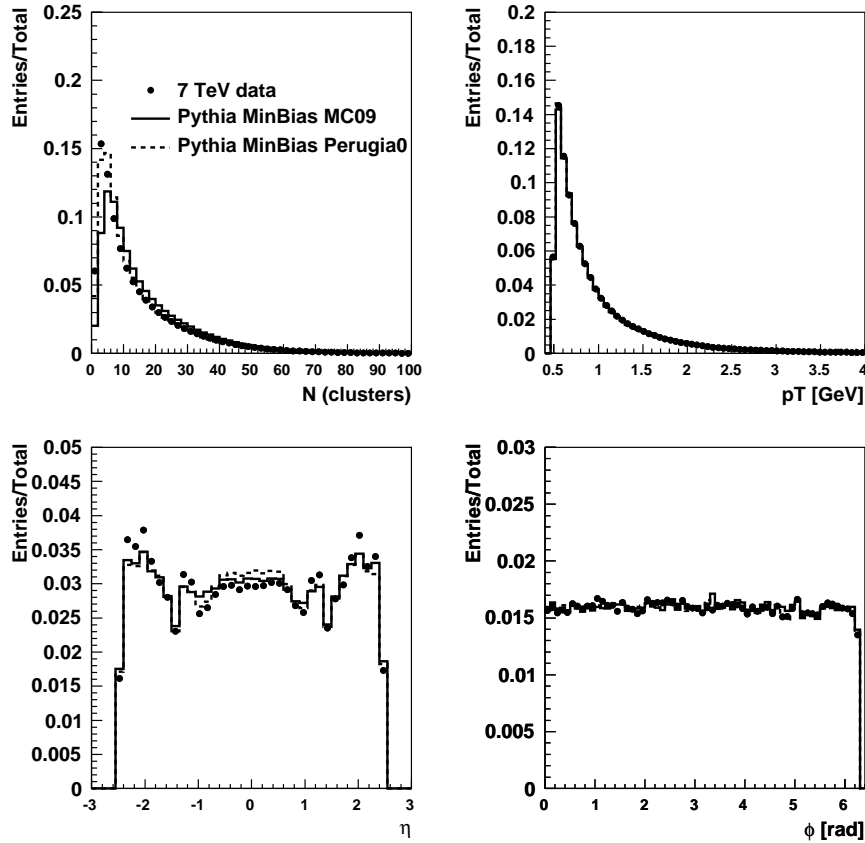


Figure 4: Topocluster properties in pp minimum bias collisions at 900 GeV compared to Monte Carlo simulation for topoclusters with $p_T > 0.5$ GeV: topocluster multiplicity, p_T distribution, η distribution and ϕ distribution. All distributions are normalized to unit area.

space regions motivated by the UE physics. Figures 5 and 6 show the shape comparisons for data and MC for p_T and η in the regions of the phase space illustrated in Fig. 1. A reasonable agreement is observed between data and the MC09 and Perugia0 PYTHIA tunes.

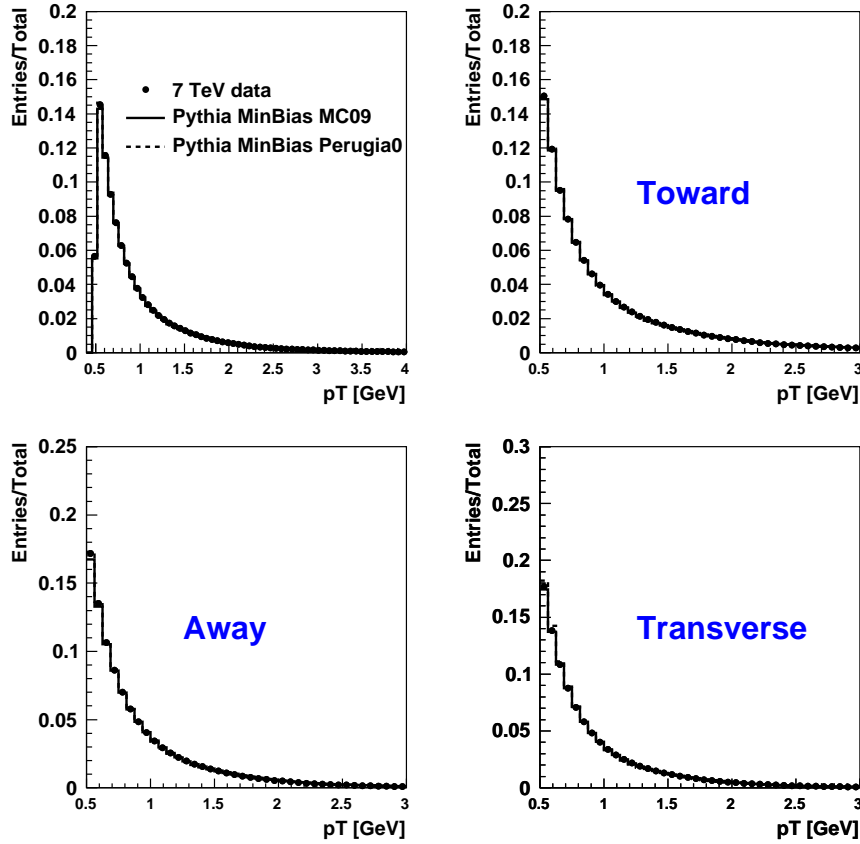


Figure 5: A comparison between data and Monte Carlo for topocluster's p_T in different regions as described in the text.

The particle densities for this analysis are defined by dividing the number of entries in a given bin by the total number of events and by the bin size, where the total number of events is calculated as the number of events which have a leading cluster with $p_T > 1$ GeV. Figure 7 shows the shape distributions in Fig. 4 transformed into particle densities as defined above. Good agreement between data and PYTHIA MC09 is still evident. PYTHIA Perugia0 shows small differences in the normalization.

As the correction for acceptance and purity is based on Monte Carlo, an essential issue is the precision with which the Monte Carlo reproduces the energy deposition in the calorimeter. This has been studied in depth using isolated tracks in minimum bias data, after extrapolating tracks to the calorimeter surface. For calibrated topoclusters, the differences between data and MC are shown in Figs. 8, 9 and 10. In average, the discrepancy between the data and MC is at the 5% level. It should be pointed out that the differences between data and MC for $\langle E/p \rangle$ in the central pseudorapidity region are larger compare to the 900 GeV data [1]. The difference between data and MC is taken into account after applying scaling factors derived from the data presented in 8 and 9 (see Sect. [?]).

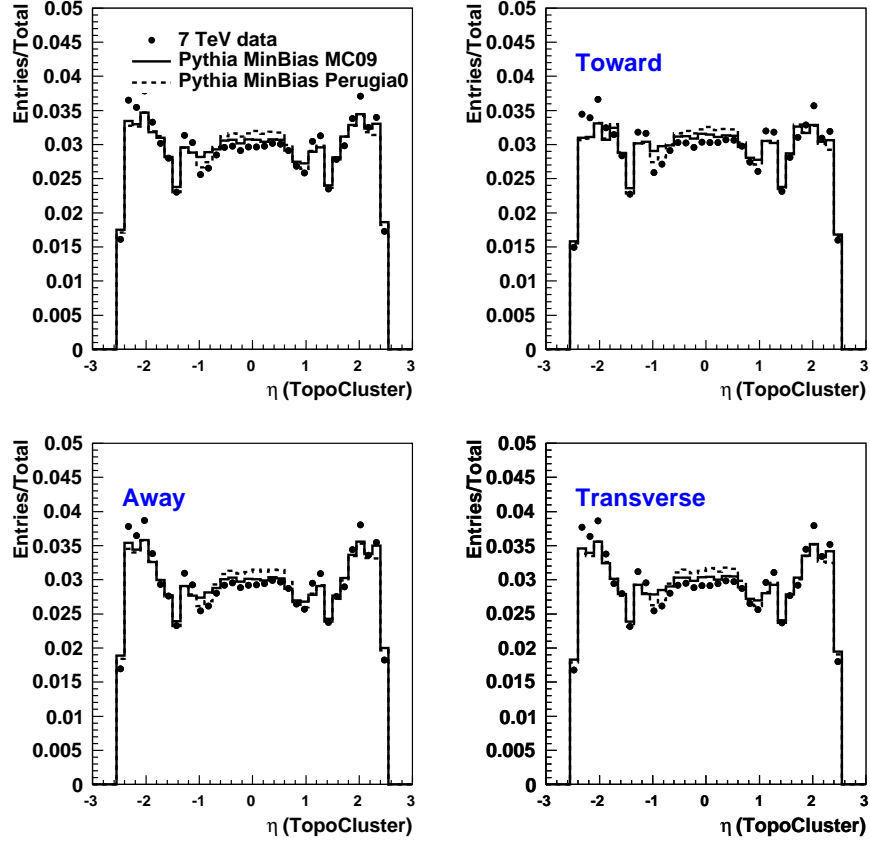


Figure 6: A comparison between data and Monte Carlo for topocluster η as described in the text.

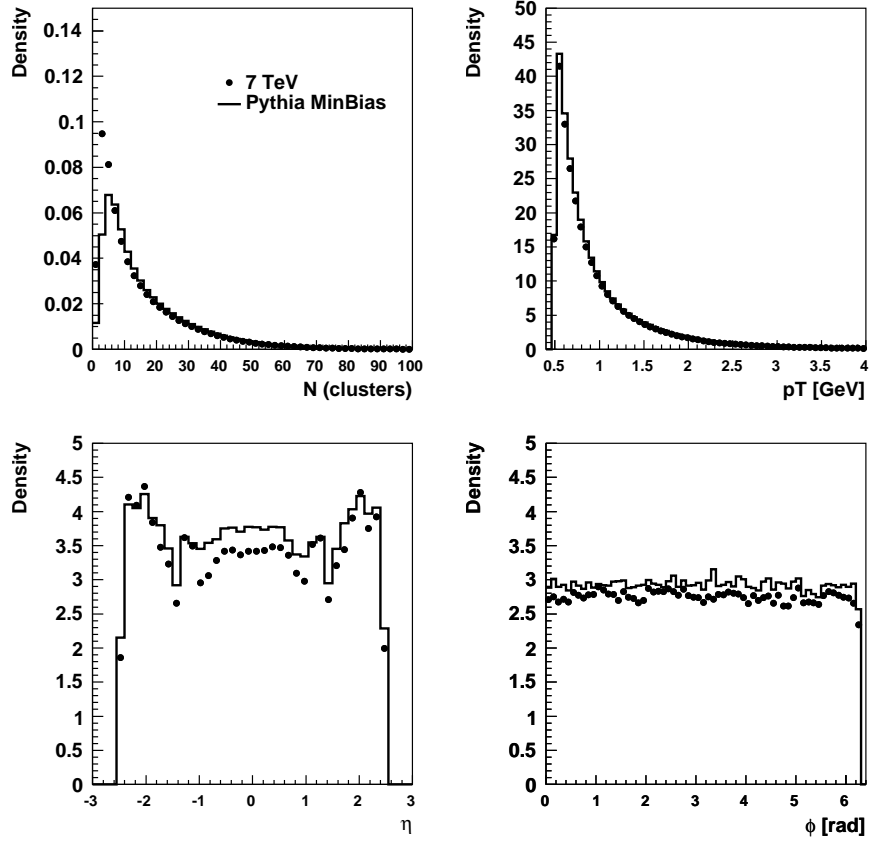


Figure 7: A comparison between data and Monte Carlo for topocluster densities as described in the text.

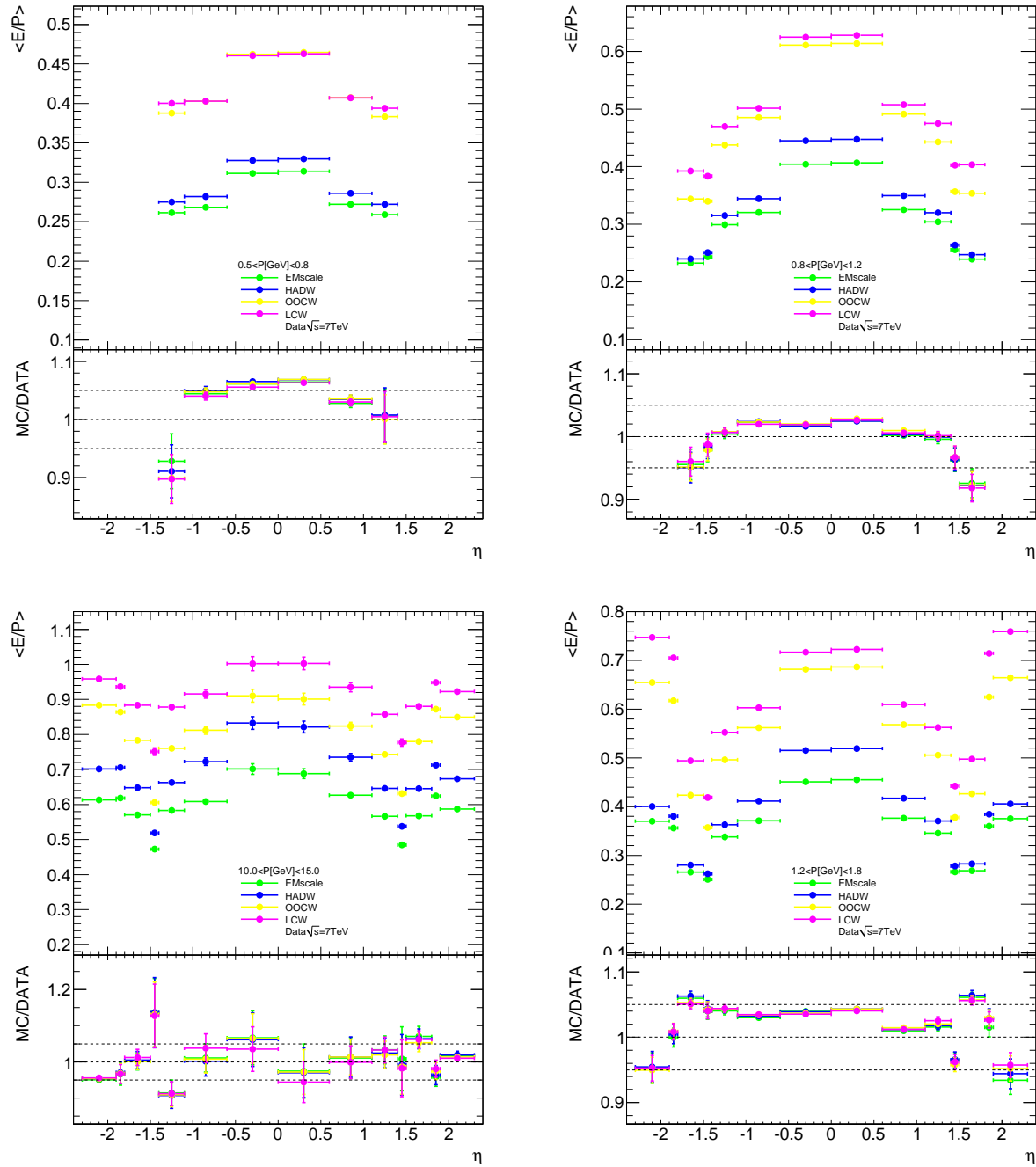


Figure 8: E/p as a function of P in different η bins for isolated tracks topoclusters matched to charged tracks in pp minimum bias events at a center of mass energy of 7 TeV. The clusters were selected after the local hadronic calibration.

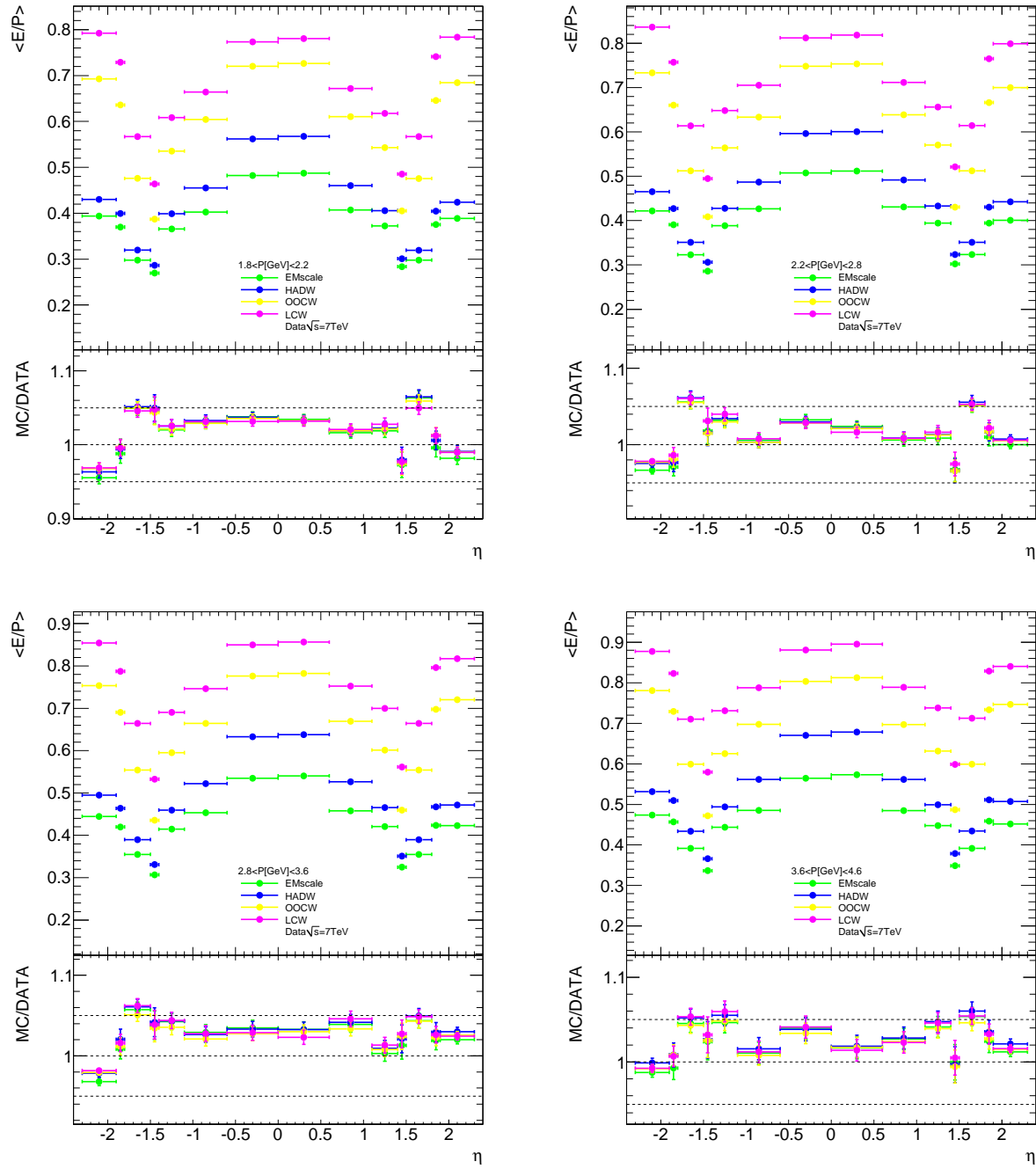


Figure 9: E/p as a function of P in different η bins for isolated tracks topoclusters matched to charged tracks in pp minimum bias events at a center of mass energy of 7 TeV. The clusters were selected after the local hadronic calibration.

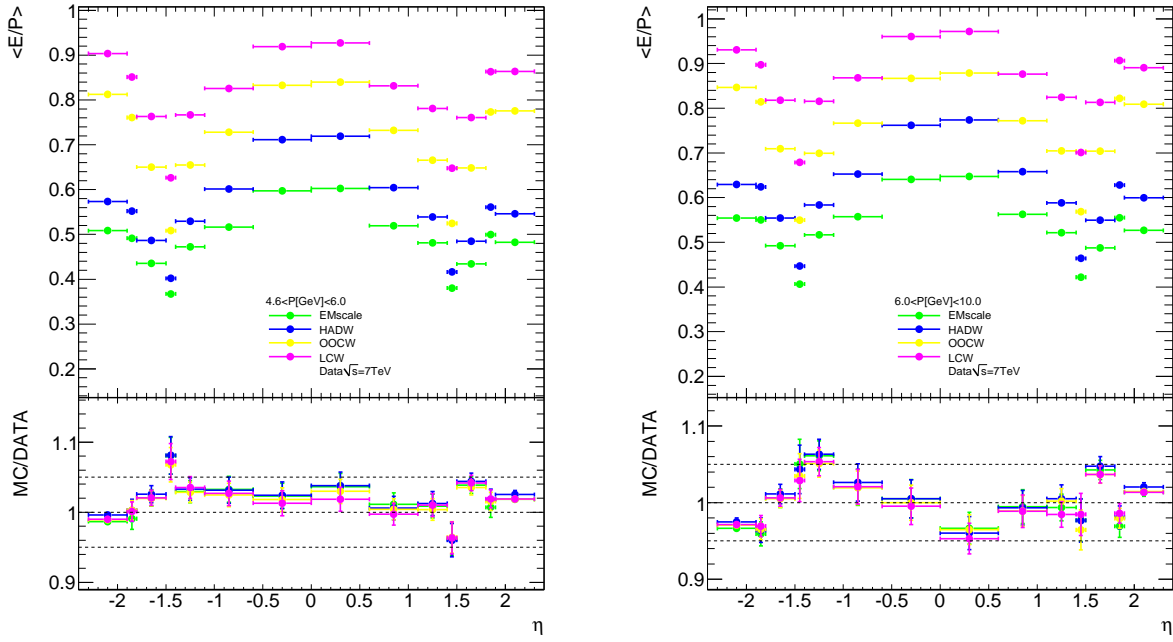


Figure 10: E/p as a function of P in different η bins for isolated tracks topoclusters matched to charged tracks in pp minimum bias events at a center of mass energy of 7 TeV. The clusters were selected after the local hadronic calibration.

5 Uncorrected distributions

As for earlier analyses [14, 15], we will study the particle density as a function of the p_T of the leading cluster in the event. Figure 11 shows the distance in azimuthal angle between the leading cluster in the event and any other cluster with $p_T > 0.5$ GeV. The cluster p_T was calculated using the calibrated energy scale (hadronic scale). A comparison was performed with the PYTHIA model after the full detector simulation. The PYTHIA model was tuned using the standard MC09 ATLAS tune and the Perugia0 tune. The density per unit of rapidity is defined as

$$\frac{N}{(\eta_{max} - \eta_{min})} \frac{1}{N_{ev} \delta\phi},$$

where N is the number of entries in the $\delta\phi$ bin of the size 0.16 rad and $\eta_{max} - \eta_{min} = 5$ represents the full pseudorapidity range and N_{ev} is the number of events triggered by a cluster with p_T above some value.

Figure 11 can be used to understand several properties of the hadronic final state in the minbias events: the birth of the leading jet as the energy scale increases, the development of a second leading jet which balances the leading jet. The width of the peak at $\delta\phi$ can be used to estimate the size of the hadronic jets at the scales defined by the $p_T(lead)$. All features of the distribution shown Figure 11 are also seen for the average p_T of calibrated topoclusters as a function of $\delta\phi$ (see Fig. 12).

Figure 13 shows the average number of topoclusters as a function of the $p_T(lead)$ of the number of topoclusters. The normalized density distributions are calculated as:

$$\frac{N}{(\eta_{max} - \eta_{min})} \frac{1}{N_{ev} \Delta\phi},$$

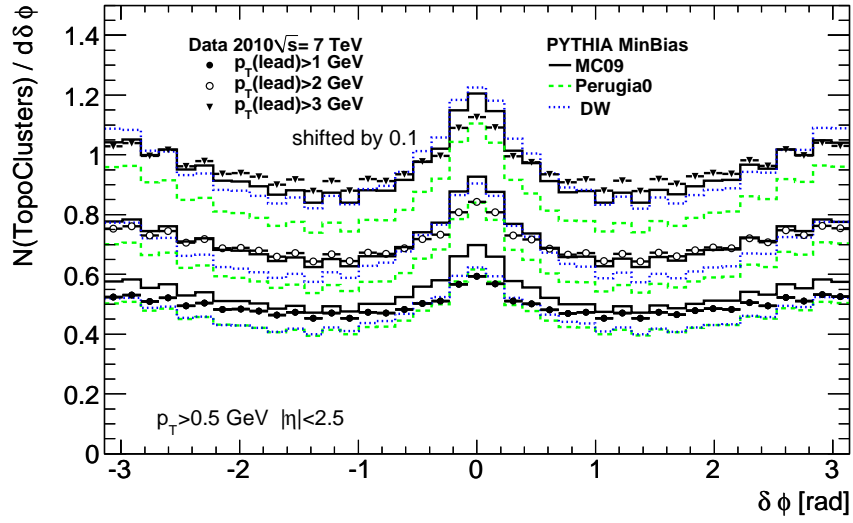


Figure 11: Cluster densities as a function of the distance in azimuthal angle between the leading cluster and any other cluster in the event. The density for $p_T(lead) > 3$ GeV was shifted by 0.1 for a better separation from the other distributions.

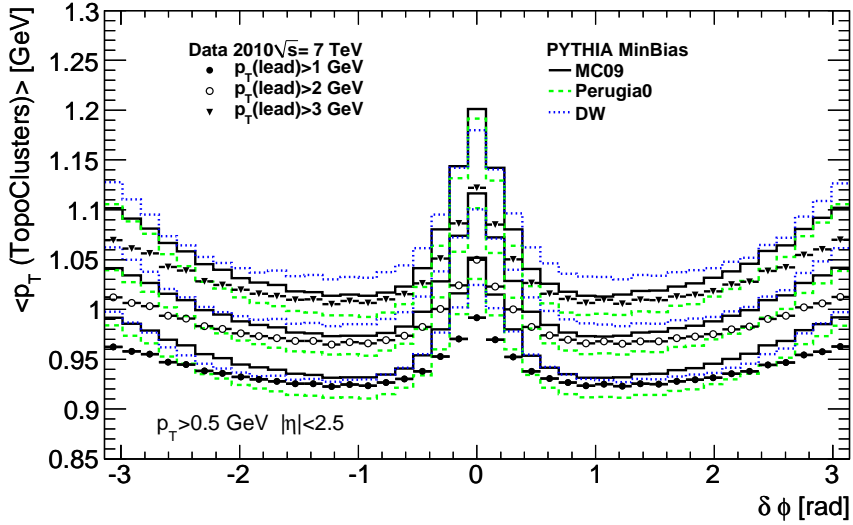


Figure 12: Average topocluster p_T as a function of the distance in azimuthal angle between the leading cluster and any other cluster in the event. The density for $p_T(lead) > 3$ GeV was shifted by 0.1 for a better separation from the other distributions.

where N is the number of entries in bins of $p_T(lead)$, N_{ev} is the number of events, and $\Delta\phi$ is the range in ϕ . In the case of the toward, away and transverse regions, $\Delta\phi = 0.33 \cdot 2\pi$ rad. Although there is rather good agreement overall, the data lies systematically above the Monte Carlo predictions in all regions.

As is the case for the $\delta\phi$ distribution, differences between data and Monte Carlo models can be seen for the average p_T of topoclusters as a function of $p_T(lead)$ (see Fig. 14). Here again, although there is generally good agreement, in this case the data lies systematically below the Monte Carlo predictions. As for the previous plot, the Perugia0 PYTHIA tune fails to describe the data, while the MC09 tune is significantly closer to the data, but still fails to describe the topocluster activity in the transverse region.

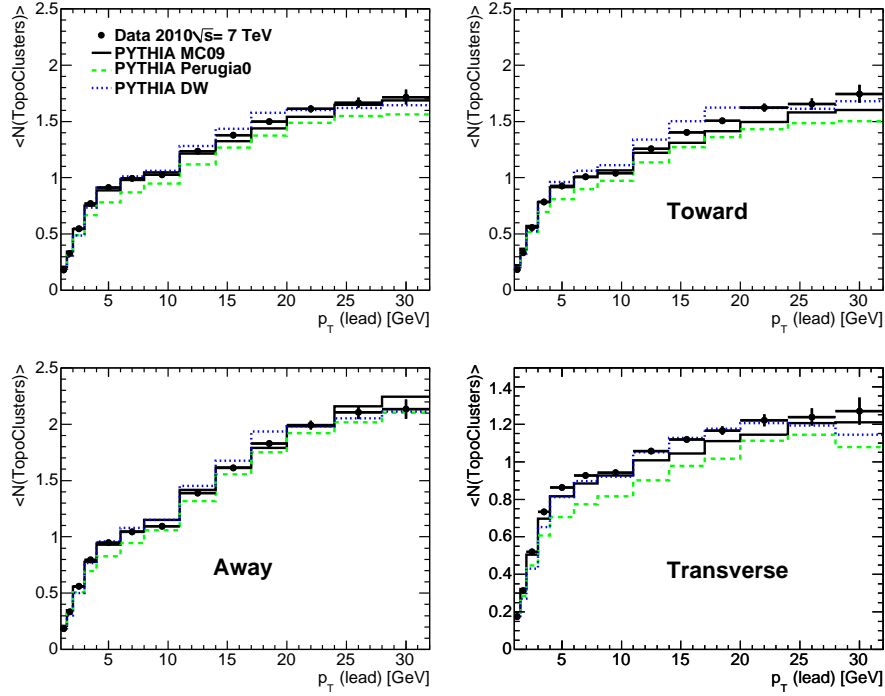


Figure 13: The average number of topoclusters per event per unit interval in η, ϕ as a function of $p_T(lead)$ for the different regions defined in Fig. 1.

Finally, Fig. 15 shows the average p_T as a function of the topocluster multiplicity. This plot is analogous to that given in Ref. [4]. It should be noted that unlike the previous distributions, the leading cluster was included in order to perform the direct comparison with the track-based distribution shown in [15] (this explains the origin of the low-multiplicity peak for the toward region). The conclusion about a good agreement with the Perugia0 tune and failure of the MC09 tune is the same as for the tracking study [4].

We will summarize this section with the following observations: 1) the reconstructed event topology is not in agreement with the discussed MC tunes. For some distributions, PYTHIA MC09 tune gives a better description (but still not perfect in the transverse region), while for others, the Perugia0 tune is in good agreement with the data; 2) the fact that all such observations are in good quantitative agreement with the tracking studies [4, 14, 15] is an indication that the topocluster observables are sensitive to the underlying physics included in the MC truth generators and are not strongly affected by systematic effects (which will be studied in this note later).

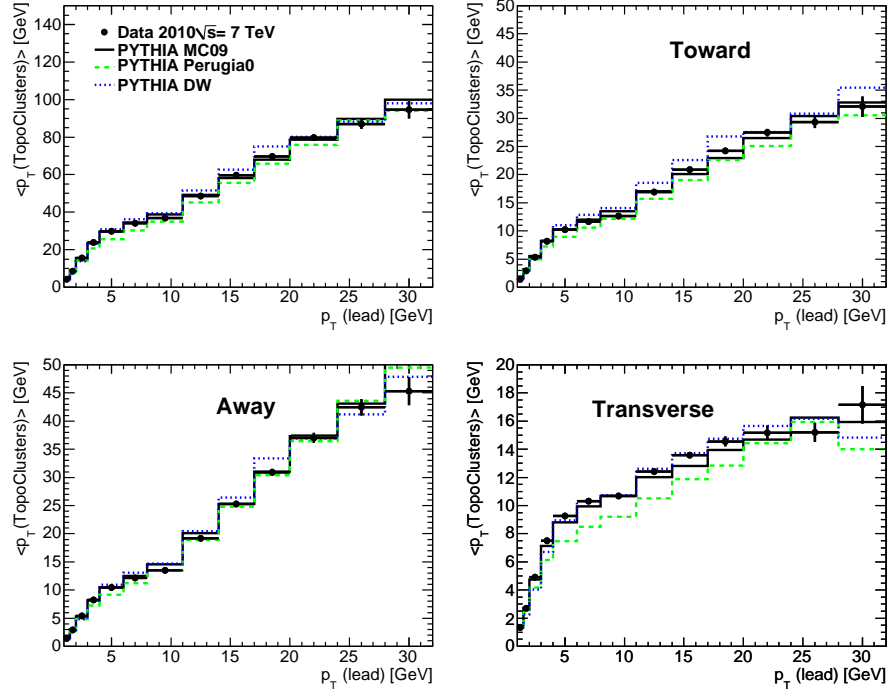


Figure 14: The average p_T of topoclusters per event per unit interval in η, ϕ as a function of $p_T(\text{lead})$ for the different regions defined in Fig. 1.

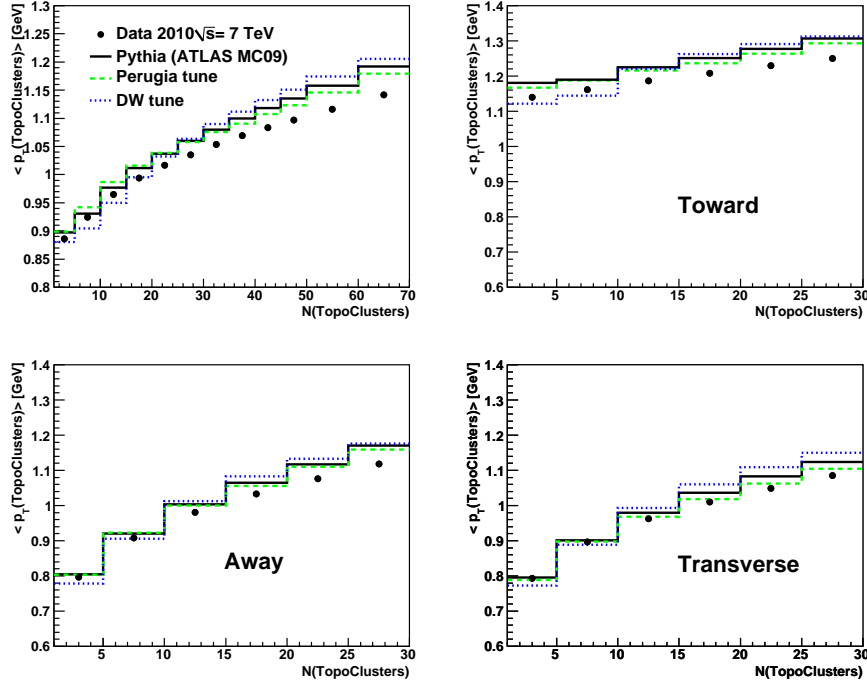


Figure 15: The average topocluster transverse momentum per event calculated using clusters with $p_T(\text{lead}) > 0.5$ GeV as a function of $p_T(\text{lead})$ for the different regions defined in Fig. 1.

6 Diffraction

To understand the contribution from diffractive events, we have used the PYTHIA MC09 models with single (SD) and double diffraction (DD) as described in Sect. 2. The minimum-bias events were mixed with the single and double diffractive events in accordance with the corresponding cross sections defined by PYTHIA.

To illustrate the contribution from diffractive events, Fig. 16 shows the visible cross section differential in p_T at the detector-level as a function of $p_T(lead)$ from 0.5 to 2 GeV. The shaded histograms show the single and double diffractive contribution to the visible cross section in PYTHIA. The diffractive contribution is at the level of 13% (SD) and 2% (DD) for $p_T(lead) > 0.5$ GeV. It decreases to 3% and 1%, respectively, for $p_T(lead) > 1$ GeV. The diffractive contribution is negligible for $p_T(lead) > 2$ GeV (below 1%). With this observation in mind, the analysis was done for $p_T(lead) > 1$ GeV where the diffractive contribution is smaller than the overall systematic uncertainty (to be discussed in Sect. 8).

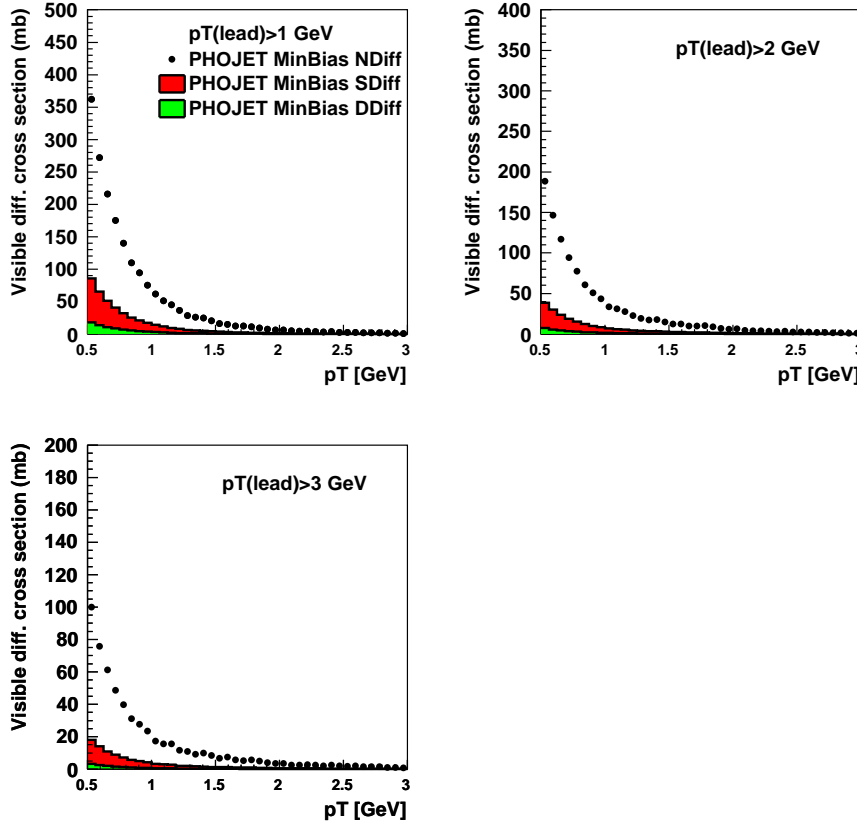


Figure 16: The visible differential cross section for calibrated topoclusters using the PYTHIA model. The largest shaded area (in red) shows the contribution from single diffraction, while the green histogram (smallest contribution) shows the contribution from double diffractive.

Unlike PYTHIA 6, the PHOJET Monte Carlo model [12] generates diffractive processes which are not restricted to low- p_T . The PHOJET model was used to calculate the densities in two steps: without diffractive events and with diffractive events (SD,DD) using the predictions for the truth cross sections. As an example, Figs. 17 and 18 show the PHOJET MC densities without diffraction (labeled as NDiff) and with diffraction (NDiff+SDiff+DDif). Diffractive events were mixed with non-diffractive events

165 using their corresponding cross sections. It can be see that the diffractive contribution is small compared
 166 to differences between different tunes.

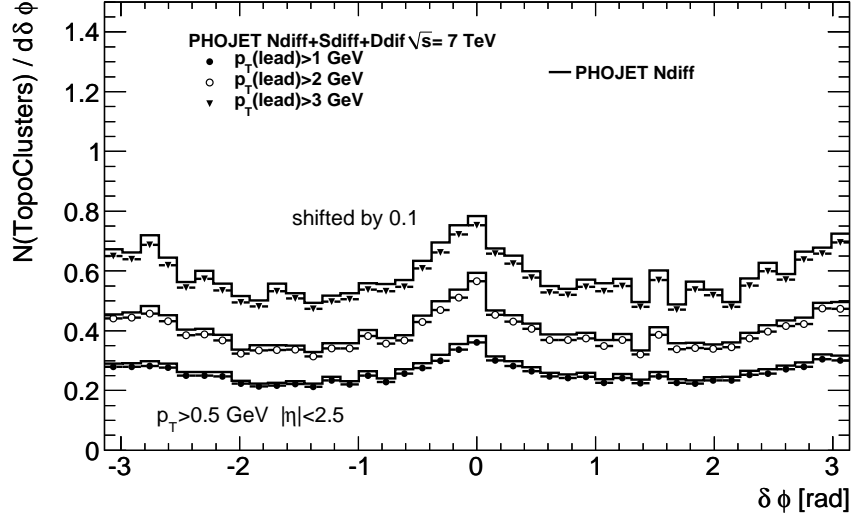


Figure 17: Cluster densities in PHOJET as a function of the distance in azimuthal angle between the leading cluster and any other cluster in the event. The density for $p_T(lead) > 3$ GeV was shifted by 0.1 for a better separation from the other distributions.

167 7 Data unfolding using bin-by-bin corrections

Due to the complexity of the measured variables, a bin-by-bin correction procedure is used to unfold the observed distributions to the hadron level. The correction factors

$$C = \frac{\mathcal{A}^{\text{gen}}}{\mathcal{A}^{\text{det}}},$$

168 are evaluated separately for each observable. In the above expression, \mathcal{A}^{gen} is calculated at the generator-
 169 level of PYTHIA MC09 and \mathcal{A}^{det} is that at the detector-level of this model. The corrected value for an
 170 observable is found by multiplying its measured value by the relevant correction factor. The correction
 171 factors thus unfold the data to the hadron level and include corrections for event selection, efficiency,
 172 purity, bin-by-bin migration, and smearing of the distributions when the leading particle is misidentified
 173 and the second leading cluster is used to set the energy scale. In the latter case, this leads a smearing of
 174 particle densities.

In the case that \mathcal{A} is a simple particle-counting observable, the bin-by-bin correction can be represented as a ratio of the purity to the reconstruction efficiency:

$$C = \rho / e,$$

where ρ is a purity calculated as the ratio:

$$\rho = \frac{N(\text{reco} \oplus \text{gen})}{N(\text{reco})},$$

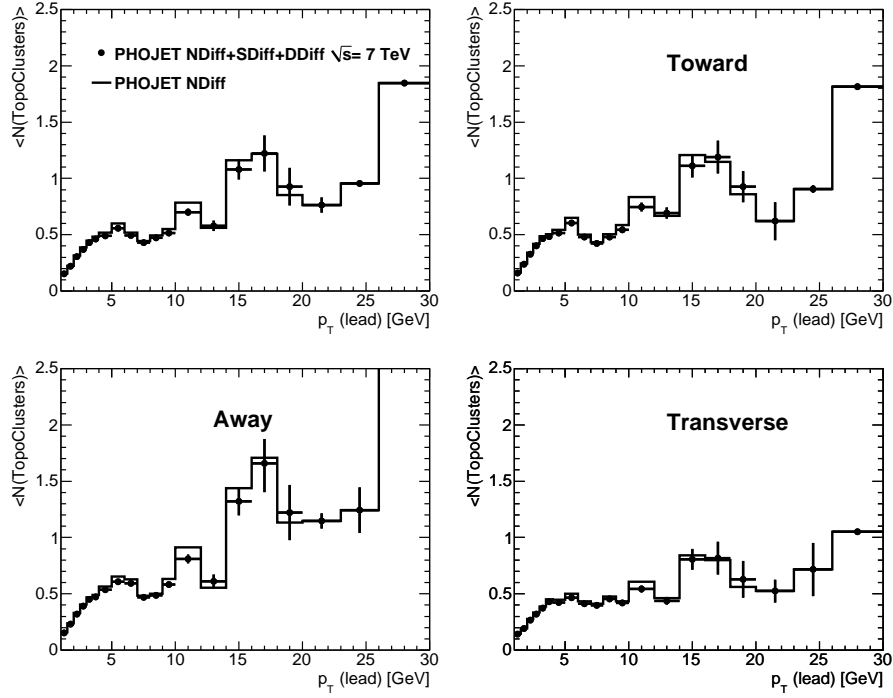


Figure 18: The average number of topoclusters per event per unit interval in η , ϕ as a function of $p_T(\text{lead})$ for the different regions defined in Fig. 1 for the PHOJET MC.

and where $N(\text{reco} \oplus \text{gen})$ is the number of reconstructed tracks which originate from truth particles generated in same bin. $N(\text{reco})$ is the number of events with reconstructed tracks counted in the same bin, irrespective of their origin. The efficiency is defined as usual:

$$e = \frac{N(\text{reco} \oplus \text{gen})}{N(\text{gen})},$$

where $N(\text{gen})$ is the number of generated truth particles in the same bin where $N(\text{reco} \oplus \text{gen})$ is reconstructed. Note that the efficiency is directly calculable and includes an event-selection and standard cluster-reconstruction efficiency. The purity correction mainly reflects smearing effects due to mismeasurement of the leading cluster used for the density calculations which are difficult to take into account. Thus the advantage of using the bin-by-bin correction is that it unfolds data in one step.

As for any detector unfolding to the hadron level, the bin-by-bin correction depends on the truth-level MC input. The model dependence affects the efficiency correction (mainly due to variations in particle types) and the purity (different underlying hadron-level distributions have different fractions of misreconstructed objects in each bin and different bin-by-bin migrations). To reduce a model dependence of the unfolding procedure, bin-by-bin migrations were minimized by using bin sizes larger than the resolutions in the bins for the distributions presented in this paper.

The model dependence can be checked by using different MC simulations of the truth level. It should be noted that a good description of the detector-level distributions is required to extract the bin-by-bin correction. This can be achieved after the re-weighting or retuning the truth-level of MC models.

Figure 19 shows the $\delta\phi$ density for all stable particles at the truth level and reconstructed topoclusters at the detector level. The ratio of those (i.e. the bin-by-bin correction factors) are shown in the bottom plot. The correction tends to increase with the increase of $p_T(\text{lead})$ as expected from the resolution effect

and since more and more clusters start to overlap in the region with large particle densities. The difference between bin-by-bin corrections extracted using different PYTHIA tunes is significantly smaller than the difference seen at the truth level of these MC tunes.

Similarly, Figure 20 shows the average p_T as a function of $\delta\phi$ for all stable particles at the truth level and reconstructed topoclusters at the detector level. The ratio of those (i.e. the bin-by-bin correction factors) are shown in the bottom figures. In this case, the measurements have small bin-by-bin corrections since they are less affected by the migration of topoclusters below the minimum p_T cut. Yet, this observable has enough sensitivity to different MC tunes as shown in Fig. 12 for the detector level.

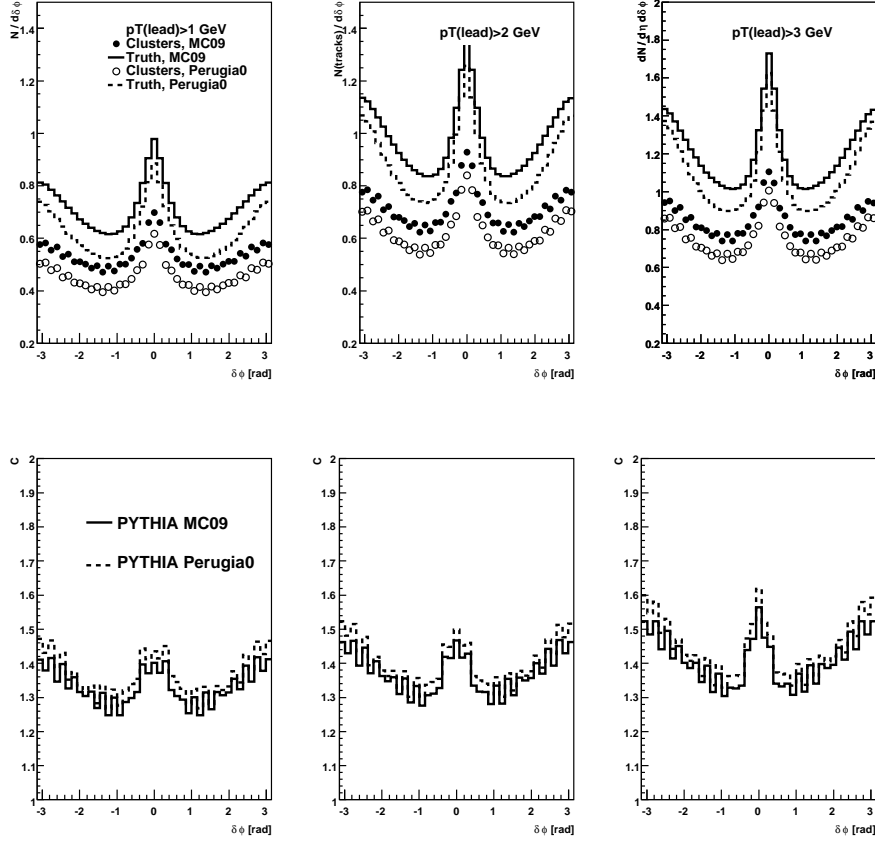


Figure 19: Densities for the truth level (stable particles) and the detector levels (calibrated topoclusters) as a function of $\delta\phi$. The bin-by-bin correction factors are shown at the bottom.

Figures 21 and 22 show the densities for all truth stable particles and calibrated topoclusters at the detector level. The corresponding detector-level distributions are shown in Figs. 13 and Fig. 14. The bin-by-bin correction factors are also shown. The correction factors are generally large and increase with p_T up to 100%. This is mainly due to the resolution effect as discussed in Sect. 4: For large p_T , there are large losses of the leading cluster and the correction factor at large $p_T(\text{lead})$ attempts to correct for such an inefficiency effect. In addition, clusters can overlap in the toward (away) regions where the density of clusters is high. The correction factors in the transverse region, which is the most interesting for the UE studies, are at the level of 50% and almost independent of p_T . Finally, Fig. 23 shows the average p_T as a function of topocluster multiplicity. The correction factors are small and almost independent of the numbers of clusters.

We will summarize this section with the following observation: unlike the tracking-based studies [14,

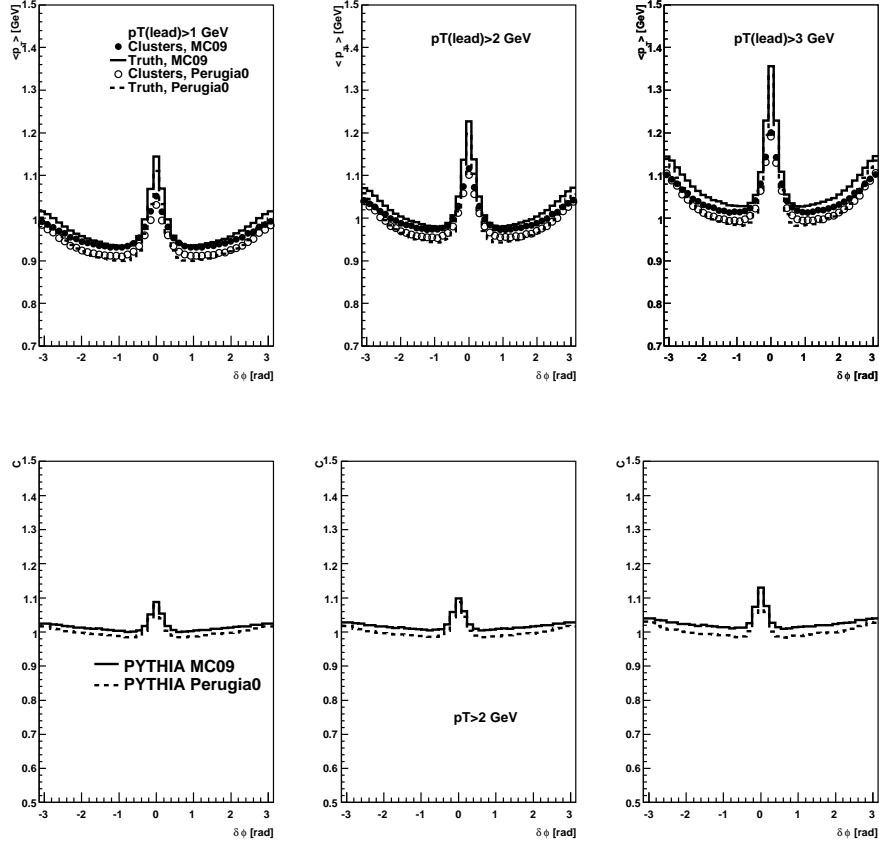


Figure 20: Average p_T for the truth level (stable particles) and the detector levels (calibrated topoclusters) as a function of $\delta\phi$. The bin-by-bin correction factors are shown at the bottom.

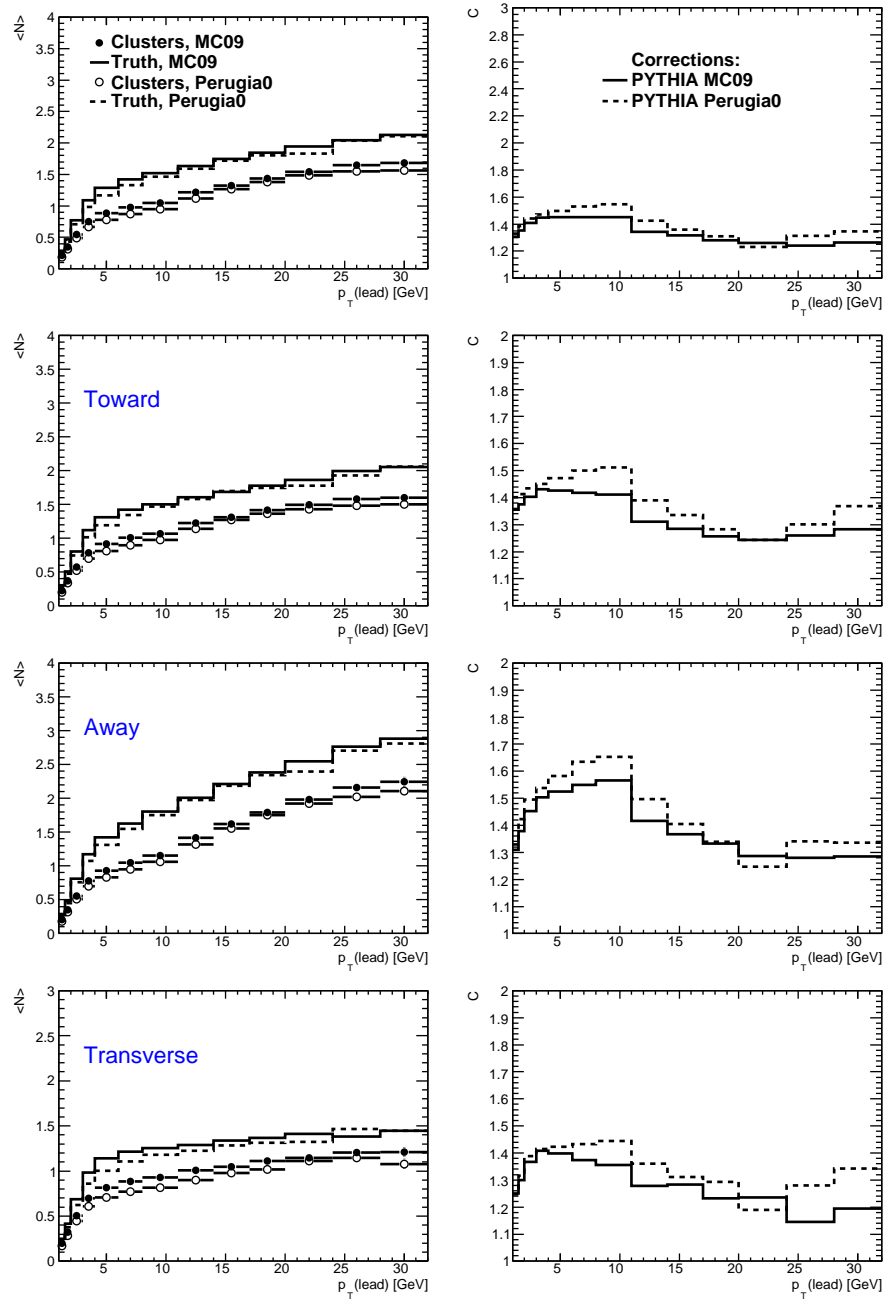


Figure 21: Densities for the truth level (charged stable particles) and the detector levels (clusters) as a function of $p_T(\text{lead})$. The bin-by-bin correction factors are shown on the right-hand side.

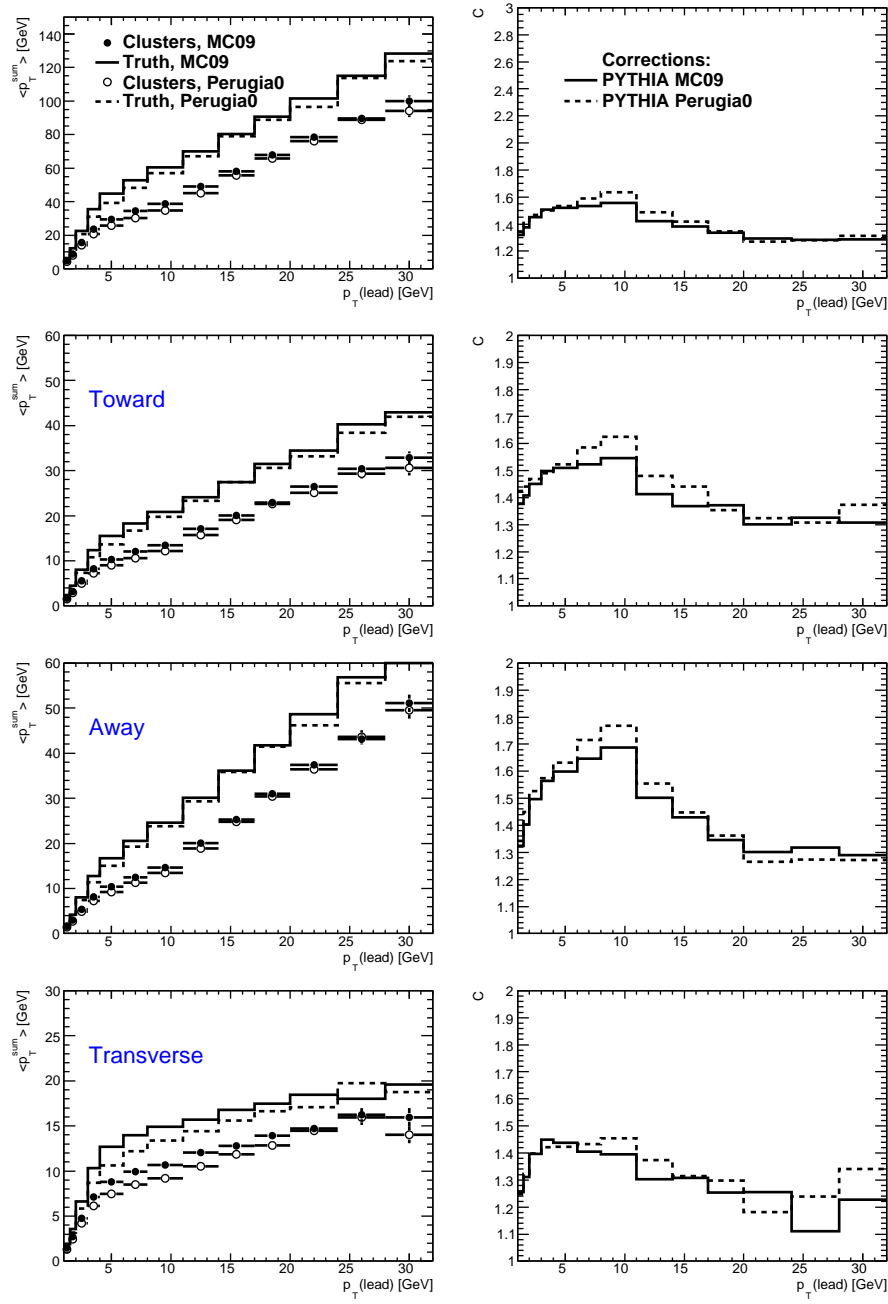


Figure 22: The average transverse momenta for the truth level (charged particles) and the detector levels (clusters) as a function of $p_T(lead)$. The bin-by-bin correction factors are shown on the right-hand side.

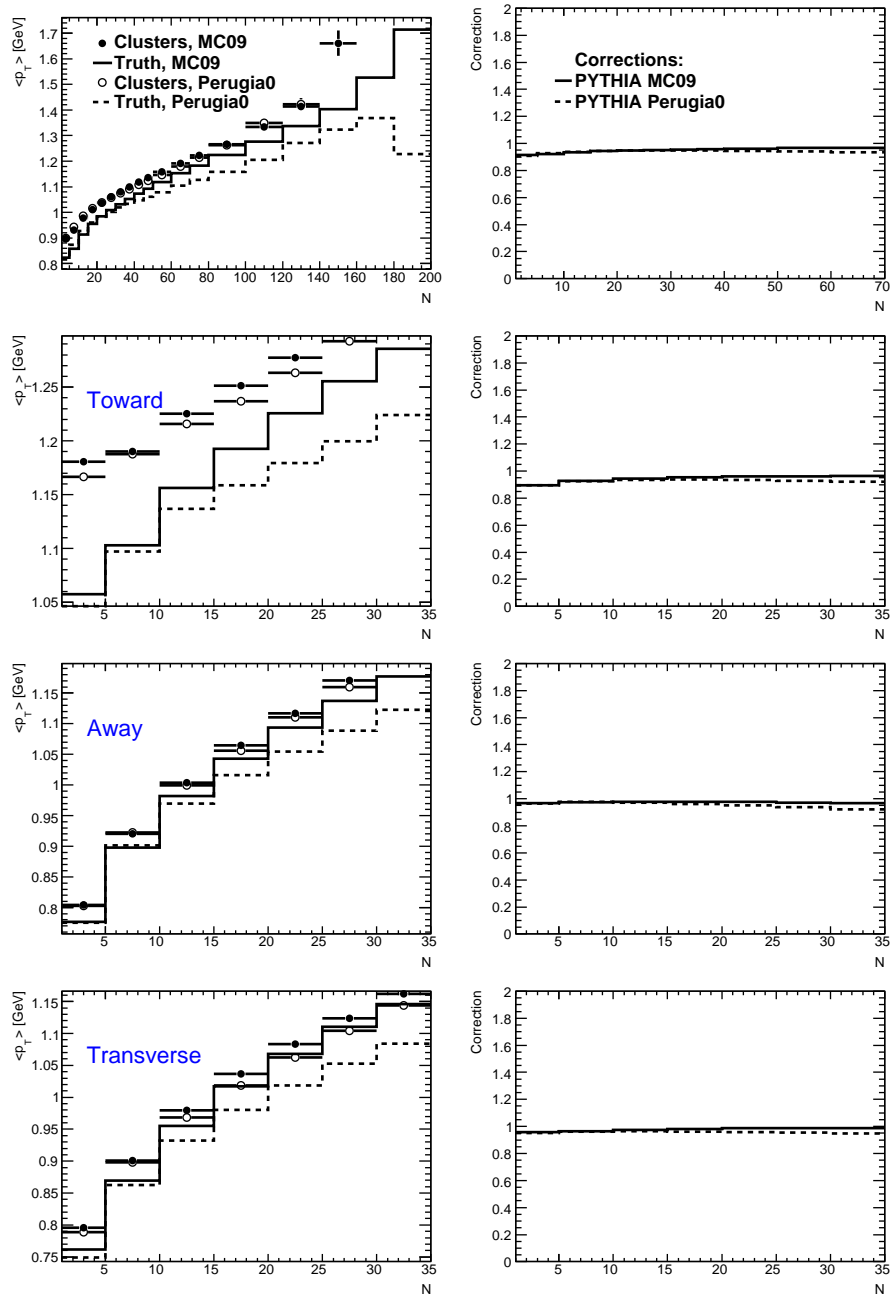


Figure 23: The average transverse momenta for the truth level and the detector levels (clusters) as a function of multiplicities. The correction factors are shown on the right-hand side.

15], the detector correction factors are larger and tend to increase with increasing p_T . For the transverse region, the correction factors are about 50%. (For the tracking studies, the bin-by-bin corrections were 20% [15]). The correction factors in the toward and the away region can reach 100% at large $p_T(lead)$. The correction factors for the measurements shown in Figs. 20 and 23 are small.

It should be noted that correction factors can be large and the measurements can still be considered to be reliable if the systematics is fully understood (large correction factors usually mean large systematics, which can easily wash out physics conclusions), and the unfolding procedure does not change physics conclusion drawn from the detector-level measurements. For the future studies, we will consider only measurements which have bin-by-bin corrections smaller than 50%.

8 Systematics

The systematic uncertainties on the measured densities were determined by changing the selection cuts or the analysis procedure and repeating the analysis. The following systematic studies have been carried out, with a typical resulting uncertainty for the given in parentheses:

- The main systematic uncertainty comes from the energy scale of calibrated topoclusters. $\pm 5\%$ energy scale uncertainty is expected for most pseudorapidity regions for the clusters at the EM-scale. Differences between the data and the MC increase to $\pm 10\%$ in the transition region ($|\eta| > 1.55$ and $|\eta| < 1.8$). On average, the energy scale uncertainty for the calibrated topoclusters is within $\pm 5\%$ for a wide range of topocluster momentum, from 0.5 to 10 GeV.
The energy scale uncertainty was taken into account by decreasing and increasing the p_T of topoclusters in the data, keeping the same topocluster p_T in the MC. The scaling factors were determined using a grid in η and P (momentum) of the tracks used for matching with topoclusters.
The energy scale uncertainty discussed above is significantly larger than the uncertainty of the event selection (including the trigger selection of the minimum bias events); [4].
- Generally, the electronic noise may not be well described by MC. This effect, however, is at the level of 10 MeV for cells, is difficult to propagate correctly to topocluster measurements, since the noise should not always be coherently added for the topocluster energies. Generally, this uncertainty is taken into account by the energy scale uncertainty discussed above.
- Positions of topocluster centers in η and ϕ were shifted by the size of one cell (± 0.025 , ± 0.025 rad) in the LArg calorimeter (less than $< 1\%$);
- Since no correction for the diffractive contribution was applied, the measurement was performed in the regions of the $p_T(lead)$ where the diffractive contribution is small (see Sect. 6). As additional systematics, all events with the number of topoclusters below 3 were removed. ($< 1\%$.);
- The bin-by-bin corrections were estimated using a MC with an extra 10% material in front of the tracking system. The extra material decreases the efficiencies and thus increases the bin-by-bin correction factor. ($+1.5\%$); In addition, a check was done using alternative detector geometry which has more material for the region $|\eta| > 2$;
- A model dependence of the bin-by-bin corrections was estimated using the alternative Perugia0 tune, as shown in Sect. 7. This corresponds to $1 - 2\%$ uncertainty. Given that the use of the PYTHIA Perugia0 model for the bin-by-bin corrections leads to small uncertainties compared to other systematics, the truth-level of this model was not re-weighted to give a proper description of the detector-level distributions.

Check	$N/d\delta\phi$	$\langle p_T \rangle$ vs N	$\langle N \rangle$ vs $p_T(lead)$
Event selection	$\pm 0.5\%$	$\pm 0.5\%$	1.5%
Energy scale	$\pm 5.1\%$	$\pm 1.5\%$	$\pm 5\%$
ϕ positions	$\pm 1.3\%$	$\pm 0.2\%$	$\pm 0.2\%$
η positions	$\pm 0.2\%$	$\pm 0.2\%$	$\pm 0.2\%$
Additional material	$\pm 0.5\%$	$\pm 0.8\%$	$\pm 1.8\%$
Model dependence	$\pm 2\%$	$\pm 1.0\%$	$\pm 1.5\%$

Table 1: A summary of systematic checks and typical contributions to the values for different types of measurements.

Table 1 summarizes the systematic uncertainties for different observables.

We did not include a possible systematic uncertainty from the PHOJET Monte Carlo model [12] since it significantly fails to describe the data at large $p_T(lead)$ [4]. For the bin-by-bin corrections, an adequate description of detector-level distributions is required, thus the truth-level of PHOJET should be re-weighted before the extraction of the bin-by-bin corrections. The PHOJET MC has exactly the same fragmentation as for PYTHIA, thus we do not expect this model to be useful for estimation of the systematical uncertainties related different modeling of the fragmentation stage. The HERWIG Monte Carlo model [16, 17] is presently unavailable.

The overall systematic uncertainty was determined by adding the above uncertainties in quadrature.

9 Results

In this section, the final results obtained after the detector corrections are discussed. Only distributions which have the smallest bin-by-bin correction factors have been used for the final measurements. As discussed before, due to significant losses of leading clusters at large $p_T(lead)$ and cluster overlaps in the regions of high particle density (the toward and away regions), the correction factors are significant. The most affected distributions are the density distributions as a function of $p_T(lead)$ and the p_T^{sum} distribution in the toward and away regions. Thus the physics conclusion for such measurements can be significantly biased towards the MC simulation used for extrapolation.

Figure 24 shows the density distribution of the particles corrected to the hadron level as a function of the distance in the azimuthal angle between the leading particle and other particles in an event. The distribution was unfolded using the bin-by-bin correction as shown in Fig. 19. The systematic uncertainties are almost fully correlated. They are shown by the green band which also includes the statistical errors added in quadrature. The data are compared to the PYTHIA truth with the MC09, Perugia0 and DW tunes. Although the general shapes of the Monte Carlo distributions are similar to that of the data, none of the three Monte Carlo tunes match the data precisely.

Figure 25 shows the average transverse momenta as a function of the distance in the azimuthal angle between the leading particle and other particles in an event. The distribution was unfolded using the bin-by-bin correction as shown in Fig. 20.

Figures 26 and 28 show the particle density and the average momenta of particles corrected to the hadron level as a function of $p_T(lead)$. Both measurements were done in the transverse region where the density of particles is not very high and thus the detector corrections are the smallest.

Figures 30 shows the average momenta as a function of charged multiplicity. The right-hand plot shows the same distribution as that discussed in Ref. [4] for tracks. As for the previous topocluster measurements, all MC tunes fail to describe the activity in the transverse region.

The tables with the detector-corrected data shown in this section are given in the "Appendices" section.

Figures 27 and 29 show the same distributions as before but compared to the 900 GeV data.

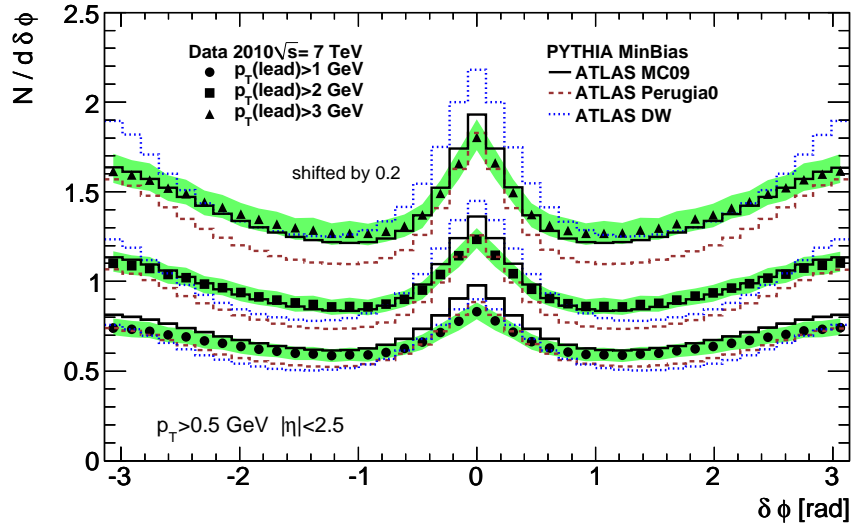


Figure 24: The density of particles per unit of pseudorapidity as a function of the distance between the leading particle and other particles in an event. The green band shows the statistical and systematical uncertainties added in quadrature. The density for $p_T(\text{lead}) > 3$ GeV is shifted by 0.2 for a better representation.

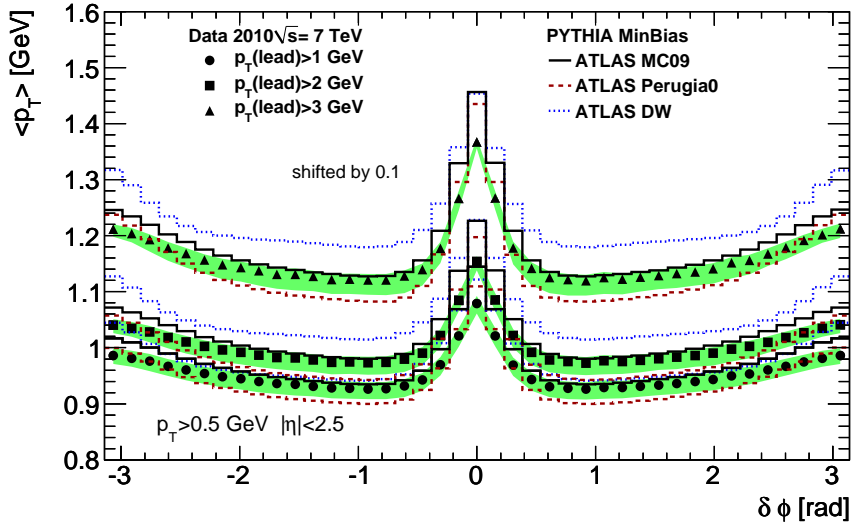


Figure 25: The average transverse momenta of particles as a function of the distance between the leading particle and other particles in an event. The green band shows the statistical and systematical uncertainties added in quadrature. The density for $p_T(\text{lead}) > 3$ GeV is shifted by 0.1.

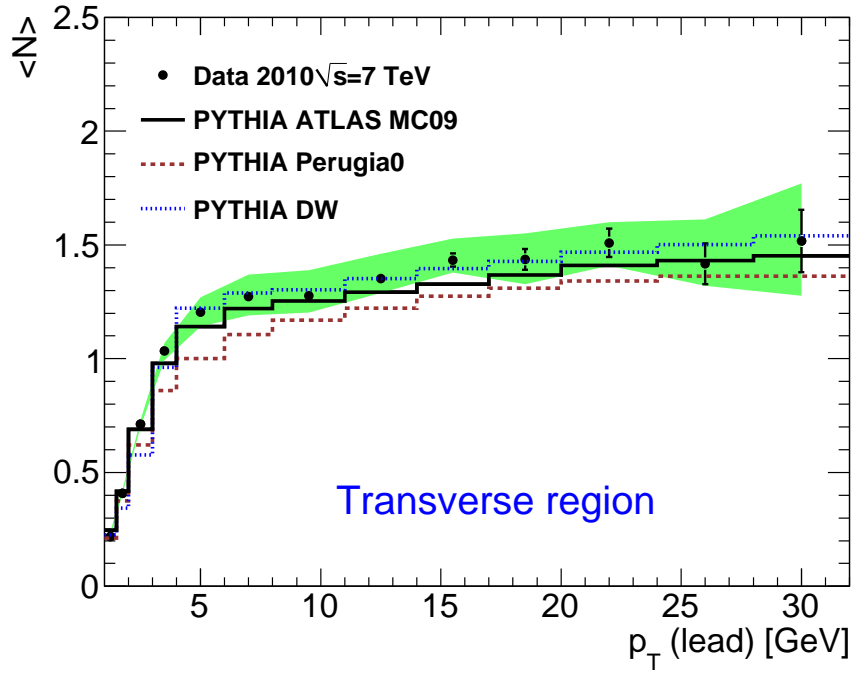


Figure 26: The average number of particles per event in one unit interval in η and ϕ as a function of the $p_T(\text{lead})$ for the transverse region indicated in Fig. 1

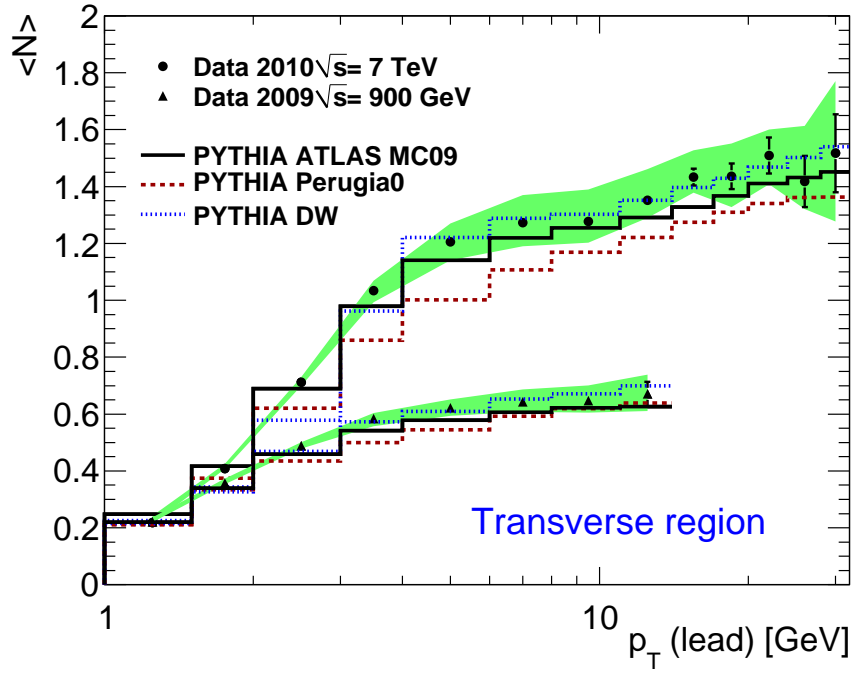


Figure 27: The average number of particles per event in one unit interval in η and ϕ as a function of the $p_T(\text{lead})$ for the transverse region indicated in Fig. 1 compared to 900 GeV data.

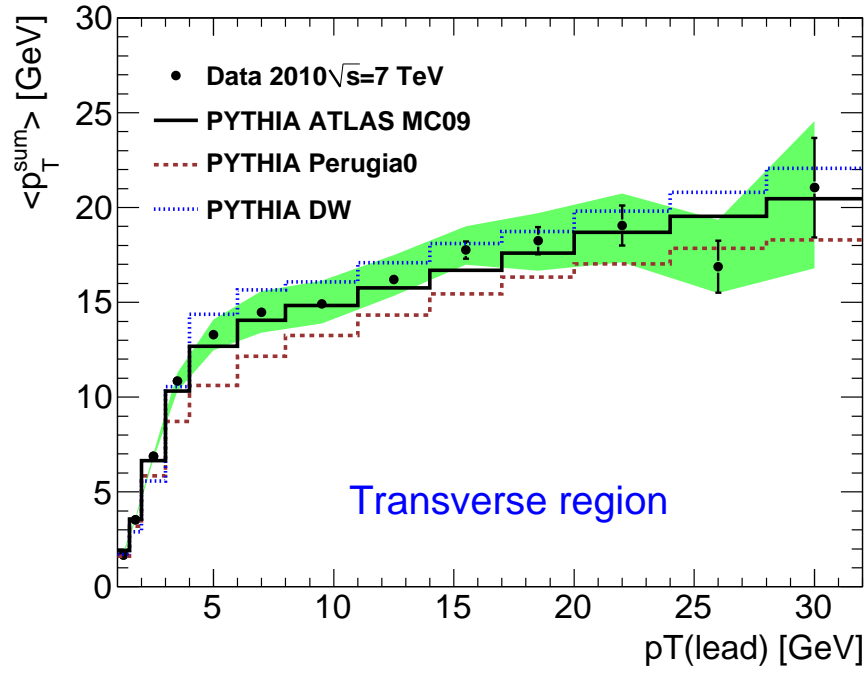


Figure 28: The average transverse momenta of particles as a function of the $p_T(\text{lead})$ for the transverse region indicated in Fig. 1.

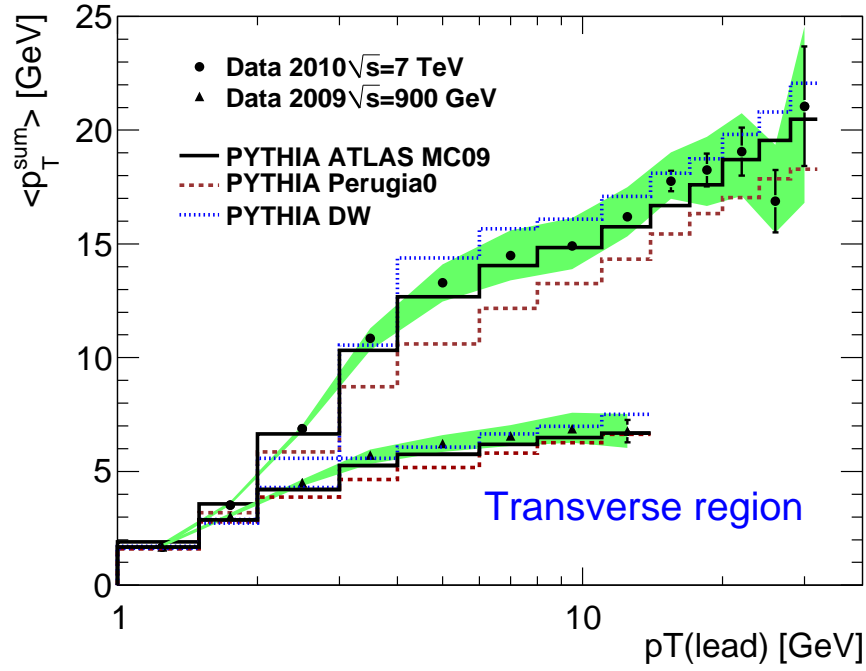


Figure 29: The average transverse momenta of particles as a function of the $p_T(\text{lead})$ for the transverse region indicated in Fig. 1 compared to 900 GeV data.

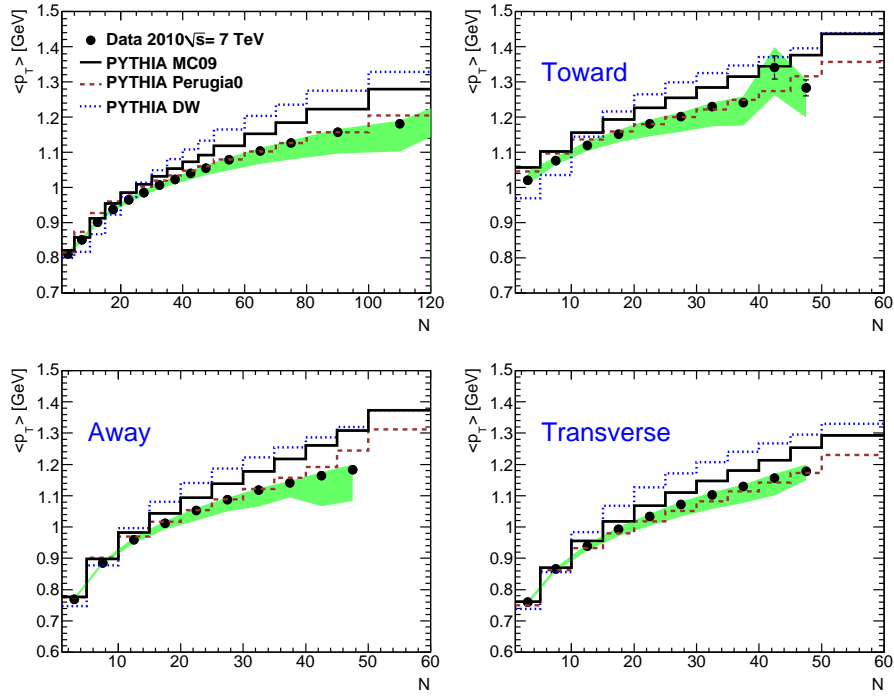


Figure 30: The average transverse momenta of particles as a function of charged-particle multiplicity for different regions of the phase space indicated in Fig. 1.

10 Summary

In this note, density and the average transverse spectra are studied and compared with the PYTHIA predictions with different tunes. All predictions fail to describe well the density distribution as a function of the azimuthal angle between the leading charged particle and any other particle in an event.

Different PYTHIA tunes fail in different extent. All Monte Carlo predictions fail to describe the particle densities as a function of $\delta\phi$. For the average transverse momentum as a function of $\delta\phi$, a good agreement is observed for PYTHIA MC09 tune, while Perugia0 and DW turn to underestimate the data.

Similarly, the lack of activity of the hadronic final state in the transverse region is seen in the density distribution and the average transverse momenta as a function of the $p_T(lead)$. For the density and the average transverse momenta as a function of the $p_T(lead)$, the DW tune is the closest to the data, while it fails to describe the average particle momentum as a function of particle multiplicity. The MC09 and the Perugia0 tunes are below the data for the particle densities. The above conclusion quantitatively agrees with that for charged particles [14, 15]. and provides a systematically independent measurement to that obtained using tracks.

References

- [1] C. Bertella et al., *Underlying event particle flow based on calorimeter clusters in pp collisions at 900 GeV with the ATLAS detector at the LHC*, Tech. Rep. ATL-COM-PHYS-2010-210, CERN, Geneva, Apr, 2010.
- [2] The ATLAS Collaboration, *Readiness of the ATLAS Tile Calorimeter for LHC Collisions*, .
- [3] The ATLAS Collaboration, G. Aad et al., *Readiness of the ATLAS Liquid Argon Calorimeter for LHC Collisions*, [arXiv:0912.2642](https://arxiv.org/abs/0912.2642) (2009) .
- [4] The ATLAS Collaboration, *Charged-particle multiplicities in pp interactions at $\sqrt{s}=900$ GeV measured with the ATLAS detector at the LHC*, [arXiv:1003.3124](https://arxiv.org/abs/1003.3124) (2010) .
- [5] NtupleMaker, *NtupleMaker package (ANL-ASC)*, .
<http://atlaswww.hep.anl.gov/asc/WebSVN/>.
- [6] T. Sjostrand, S. Mrenna, and P. Z. Skands, *PYTHIA 6.4 Physics and Manual*, JHEP **05** (2006) 026, [arXiv:hep-ph/0603175](https://arxiv.org/abs/hep-ph/0603175).
- [7] *ATLAS Monte Carlo tunes for MC09*, Tech. Rep. ATL-PHYS-PUB-2010-002. ATL-COM-PHYS-2010-033, CERN, Geneva, Mar, 2010.
- [8] A. Sherstnev and R. S. Thorne, *Parton Distributions for LO Generators*, Eur. Phys. J. **C55** (2008) 553–575, [arXiv:0711.2473](https://arxiv.org/abs/0711.2473) [hep-ph].
- [9] F. Abe et al., *Transverse-momentum distributions of charged particles produced in pp interactions at 630 and 1800 GeV*, Phys. Rev. Lett. **61** (1988) no. 16, 1819.
- [10] P. Z. Skands, *The Perugia Tunes*, [arXiv:0905.3418](https://arxiv.org/abs/0905.3418) [hep-ph].
- [11] R. Field, *MinBias and the Underlying Event at the Tevatron and the LHC*, A talk presented at the Fermilab mc tuning workshop, tech. rep., FERMILAB, 2002.
- [12] R. Engel and J. Ranft, *Color singlet exchange between jets and the PHOJET Monte Carlo*, Nucl. Phys. Proc. Suppl. **75A** (1999) 272–274.
- [13] NtupleMakerTruth, *NtupleMakerTruth package (ANL-ASC)*, .
<http://atlaswww.hep.anl.gov/asc/WebSVN/>.
- [14] The ATLAS Collaboration, A. Buckley et al., *Track-based underlying event measurements in pp collisions at $\sqrt{s} = 900$ GeV with the ATLAS detector at the LHC*, ATL-COM-PHYS-2010-164 (2010) .
- [15] The ATLAS Collaboration, A. Buckley et al., *Using bin-by-bin corrections for track-based underlying event measurements in pp collisions at 900 GeV*, ATL-COM-PHYS-2010-165 (2010) .
- [16] G. Corcella et al., *HERWIG 6.5: an event generator for Hadron Emission Reactions With Interfering Gluons (including supersymmetric processes)*, JHEP **01** (2001) 010, [arXiv:hep-ph/0011363](https://arxiv.org/abs/hep-ph/0011363).
- [17] G. Corcella et al., *HERWIG 6.5 release note*, [arXiv:hep-ph/0210213](https://arxiv.org/abs/hep-ph/0210213).

337 **Appendices**

338 **A Tables for the figures of Sect. 9.**

$N/d\delta\phi$ vs $\delta\phi$						
	$p_T(lead) > 1 \text{ GeV}$		$p_T(lead) > 2 \text{ GeV}$		$p_T(lead) > 3 \text{ GeV}$	
bin center	value	error	value	error	value	error
-3.063	0.740	$\pm 0.001^{+0.053}_{-0.040}$	1.101	$\pm 0.001^{+0.053}_{-0.047}$	1.614	$\pm 0.002^{+0.053}_{-0.065}$
-2.910	0.733	$\pm 0.001^{+0.047}_{-0.044}$	1.089	$\pm 0.001^{+0.047}_{-0.053}$	1.594	$\pm 0.002^{+0.047}_{-0.074}$
-2.757	0.722	$\pm 0.001^{+0.052}_{-0.039}$	1.071	$\pm 0.001^{+0.052}_{-0.044}$	1.566	$\pm 0.002^{+0.052}_{-0.062}$
-2.604	0.701	$\pm 0.001^{+0.043}_{-0.042}$	1.038	$\pm 0.001^{+0.043}_{-0.050}$	1.520	$\pm 0.002^{+0.043}_{-0.071}$
-2.451	0.691	$\pm 0.001^{+0.046}_{-0.038}$	1.021	$\pm 0.001^{+0.046}_{-0.043}$	1.489	$\pm 0.002^{+0.046}_{-0.061}$
-2.298	0.668	$\pm 0.001^{+0.039}_{-0.042}$	0.986	$\pm 0.001^{+0.039}_{-0.052}$	1.443	$\pm 0.002^{+0.039}_{-0.074}$
-2.144	0.655	$\pm 0.001^{+0.041}_{-0.036}$	0.966	$\pm 0.001^{+0.041}_{-0.042}$	1.413	$\pm 0.002^{+0.041}_{-0.060}$
-1.991	0.637	$\pm 0.001^{+0.038}_{-0.040}$	0.938	$\pm 0.001^{+0.038}_{-0.049}$	1.375	$\pm 0.002^{+0.038}_{-0.069}$
-1.838	0.623	$\pm 0.001^{+0.036}_{-0.038}$	0.915	$\pm 0.001^{+0.036}_{-0.046}$	1.347	$\pm 0.002^{+0.036}_{-0.065}$
-1.685	0.611	$\pm 0.001^{+0.040}_{-0.035}$	0.896	$\pm 0.001^{+0.040}_{-0.041}$	1.321	$\pm 0.002^{+0.040}_{-0.057}$
-1.532	0.600	$\pm 0.001^{+0.035}_{-0.038}$	0.879	$\pm 0.001^{+0.035}_{-0.047}$	1.299	$\pm 0.002^{+0.035}_{-0.066}$
-1.379	0.595	$\pm 0.001^{+0.040}_{-0.034}$	0.872	$\pm 0.001^{+0.040}_{-0.039}$	1.286	$\pm 0.002^{+0.040}_{-0.056}$
-1.225	0.587	$\pm 0.001^{+0.035}_{-0.037}$	0.859	$\pm 0.001^{+0.035}_{-0.046}$	1.269	$\pm 0.002^{+0.035}_{-0.065}$
-1.072	0.590	$\pm 0.001^{+0.040}_{-0.034}$	0.860	$\pm 0.001^{+0.040}_{-0.039}$	1.269	$\pm 0.002^{+0.040}_{-0.055}$
-0.919	0.591	$\pm 0.001^{+0.036}_{-0.038}$	0.858	$\pm 0.001^{+0.036}_{-0.046}$	1.268	$\pm 0.002^{+0.036}_{-0.065}$
-0.766	0.605	$\pm 0.001^{+0.041}_{-0.035}$	0.874	$\pm 0.001^{+0.041}_{-0.042}$	1.279	$\pm 0.002^{+0.041}_{-0.058}$
-0.613	0.627	$\pm 0.001^{+0.041}_{-0.036}$	0.901	$\pm 0.001^{+0.041}_{-0.043}$	1.308	$\pm 0.002^{+0.041}_{-0.059}$
-0.460	0.661	$\pm 0.001^{+0.042}_{-0.043}$	0.953	$\pm 0.001^{+0.042}_{-0.053}$	1.371	$\pm 0.002^{+0.042}_{-0.073}$
-0.306	0.714	$\pm 0.001^{+0.048}_{-0.038}$	1.039	$\pm 0.001^{+0.048}_{-0.043}$	1.491	$\pm 0.002^{+0.048}_{-0.059}$
-0.153	0.778	$\pm 0.001^{+0.047}_{-0.052}$	1.143	$\pm 0.001^{+0.047}_{-0.064}$	1.656	$\pm 0.002^{+0.047}_{-0.087}$
-0.000	0.832	$\pm 0.001^{+0.052}_{-0.043}$	1.235	$\pm 0.002^{+0.052}_{-0.049}$	1.805	$\pm 0.002^{+0.052}_{-0.072}$
0.153	0.780	$\pm 0.001^{+0.048}_{-0.053}$	1.146	$\pm 0.001^{+0.048}_{-0.065}$	1.661	$\pm 0.002^{+0.048}_{-0.089}$
0.306	0.718	$\pm 0.001^{+0.048}_{-0.038}$	1.044	$\pm 0.001^{+0.048}_{-0.043}$	1.497	$\pm 0.002^{+0.048}_{-0.061}$
0.460	0.663	$\pm 0.001^{+0.043}_{-0.043}$	0.956	$\pm 0.001^{+0.043}_{-0.053}$	1.374	$\pm 0.002^{+0.043}_{-0.072}$
0.613	0.628	$\pm 0.001^{+0.041}_{-0.037}$	0.904	$\pm 0.001^{+0.041}_{-0.043}$	1.313	$\pm 0.002^{+0.041}_{-0.059}$
0.766	0.606	$\pm 0.001^{+0.041}_{-0.036}$	0.876	$\pm 0.001^{+0.041}_{-0.042}$	1.284	$\pm 0.002^{+0.041}_{-0.059}$
0.919	0.593	$\pm 0.001^{+0.036}_{-0.038}$	0.860	$\pm 0.001^{+0.036}_{-0.047}$	1.268	$\pm 0.002^{+0.036}_{-0.065}$
1.072	0.590	$\pm 0.001^{+0.040}_{-0.034}$	0.860	$\pm 0.001^{+0.040}_{-0.039}$	1.269	$\pm 0.002^{+0.040}_{-0.055}$
1.225	0.588	$\pm 0.001^{+0.035}_{-0.037}$	0.858	$\pm 0.001^{+0.035}_{-0.045}$	1.271	$\pm 0.002^{+0.035}_{-0.063}$
1.379	0.596	$\pm 0.001^{+0.040}_{-0.034}$	0.871	$\pm 0.001^{+0.040}_{-0.040}$	1.286	$\pm 0.002^{+0.040}_{-0.057}$
1.532	0.599	$\pm 0.001^{+0.035}_{-0.038}$	0.879	$\pm 0.001^{+0.035}_{-0.047}$	1.298	$\pm 0.002^{+0.035}_{-0.066}$
1.685	0.612	$\pm 0.001^{+0.040}_{-0.035}$	0.897	$\pm 0.001^{+0.040}_{-0.041}$	1.321	$\pm 0.002^{+0.040}_{-0.059}$
1.838	0.625	$\pm 0.001^{+0.037}_{-0.038}$	0.918	$\pm 0.001^{+0.037}_{-0.046}$	1.349	$\pm 0.002^{+0.037}_{-0.066}$
1.991	0.637	$\pm 0.001^{+0.038}_{-0.040}$	0.936	$\pm 0.001^{+0.038}_{-0.049}$	1.370	$\pm 0.002^{+0.038}_{-0.069}$
2.144	0.654	$\pm 0.001^{+0.041}_{-0.036}$	0.963	$\pm 0.001^{+0.041}_{-0.042}$	1.410	$\pm 0.002^{+0.041}_{-0.059}$
2.298	0.670	$\pm 0.001^{+0.038}_{-0.043}$	0.988	$\pm 0.001^{+0.038}_{-0.054}$	1.445	$\pm 0.002^{+0.038}_{-0.075}$
2.451	0.689	$\pm 0.001^{+0.046}_{-0.037}$	1.020	$\pm 0.001^{+0.046}_{-0.043}$	1.488	$\pm 0.002^{+0.046}_{-0.061}$
2.604	0.704	$\pm 0.001^{+0.042}_{-0.042}$	1.041	$\pm 0.001^{+0.042}_{-0.051}$	1.523	$\pm 0.002^{+0.042}_{-0.071}$
2.757	0.724	$\pm 0.001^{+0.050}_{-0.039}$	1.074	$\pm 0.001^{+0.050}_{-0.044}$	1.568	$\pm 0.002^{+0.050}_{-0.063}$
2.910	0.733	$\pm 0.001^{+0.047}_{-0.044}$	1.090	$\pm 0.001^{+0.047}_{-0.053}$	1.598	$\pm 0.002^{+0.047}_{-0.075}$
3.063	0.742	$\pm 0.001^{+0.051}_{-0.041}$	1.102	$\pm 0.001^{+0.051}_{-0.047}$	1.616	$\pm 0.002^{+0.051}_{-0.066}$

Table 2: The density of particles per unit of pseudorapidity as a function of the distance between the leading particle and other particles in an event, see Fig. 24. The statistical and systematical uncertainties are given separately.

$\langle p_T \rangle$ vs $\delta\phi$						
	$p_T(lead) > 1 \text{ GeV}$		$p_T(lead) > 2 \text{ GeV}$		$p_T(lead) > 3 \text{ GeV}$	
bin center	value	error	value	error	value	error
-3.063	0.986	$\pm 0.001^{+0.013}_{-0.015}$	1.040	$\pm 0.001^{+0.013}_{-0.014}$	1.212	$\pm 0.001^{+0.013}_{-0.013}$
-2.910	0.981	$\pm 0.001^{+0.013}_{-0.015}$	1.035	$\pm 0.001^{+0.013}_{-0.015}$	1.203	$\pm 0.001^{+0.013}_{-0.015}$
-2.757	0.976	$\pm 0.001^{+0.013}_{-0.017}$	1.028	$\pm 0.001^{+0.013}_{-0.019}$	1.193	$\pm 0.001^{+0.013}_{-0.022}$
-2.604	0.967	$\pm 0.001^{+0.013}_{-0.017}$	1.018	$\pm 0.001^{+0.013}_{-0.019}$	1.178	$\pm 0.001^{+0.013}_{-0.022}$
-2.451	0.961	$\pm 0.001^{+0.013}_{-0.019}$	1.010	$\pm 0.001^{+0.013}_{-0.021}$	1.168	$\pm 0.001^{+0.013}_{-0.025}$
-2.298	0.954	$\pm 0.001^{+0.012}_{-0.018}$	1.003	$\pm 0.001^{+0.012}_{-0.020}$	1.157	$\pm 0.001^{+0.012}_{-0.024}$
-2.144	0.948	$\pm 0.001^{+0.012}_{-0.019}$	0.996	$\pm 0.001^{+0.012}_{-0.021}$	1.148	$\pm 0.001^{+0.012}_{-0.026}$
-1.991	0.945	$\pm 0.001^{+0.012}_{-0.019}$	0.992	$\pm 0.001^{+0.012}_{-0.021}$	1.143	$\pm 0.001^{+0.012}_{-0.025}$
-1.838	0.940	$\pm 0.001^{+0.012}_{-0.019}$	0.987	$\pm 0.001^{+0.012}_{-0.022}$	1.137	$\pm 0.001^{+0.012}_{-0.027}$
-1.685	0.936	$\pm 0.001^{+0.012}_{-0.019}$	0.983	$\pm 0.001^{+0.012}_{-0.021}$	1.131	$\pm 0.001^{+0.012}_{-0.026}$
-1.532	0.935	$\pm 0.001^{+0.012}_{-0.020}$	0.982	$\pm 0.001^{+0.012}_{-0.023}$	1.131	$\pm 0.001^{+0.012}_{-0.029}$
-1.379	0.931	$\pm 0.001^{+0.012}_{-0.018}$	0.978	$\pm 0.001^{+0.012}_{-0.021}$	1.127	$\pm 0.001^{+0.012}_{-0.026}$
-1.225	0.928	$\pm 0.001^{+0.012}_{-0.019}$	0.974	$\pm 0.001^{+0.012}_{-0.021}$	1.122	$\pm 0.001^{+0.012}_{-0.026}$
-1.072	0.928	$\pm 0.001^{+0.012}_{-0.019}$	0.975	$\pm 0.001^{+0.012}_{-0.021}$	1.122	$\pm 0.001^{+0.012}_{-0.026}$
-0.919	0.926	$\pm 0.001^{+0.012}_{-0.018}$	0.973	$\pm 0.001^{+0.012}_{-0.021}$	1.121	$\pm 0.001^{+0.012}_{-0.027}$
-0.766	0.927	$\pm 0.001^{+0.012}_{-0.019}$	0.974	$\pm 0.001^{+0.012}_{-0.022}$	1.121	$\pm 0.001^{+0.012}_{-0.027}$
-0.613	0.932	$\pm 0.001^{+0.013}_{-0.020}$	0.980	$\pm 0.001^{+0.013}_{-0.023}$	1.128	$\pm 0.001^{+0.013}_{-0.030}$
-0.460	0.942	$\pm 0.001^{+0.013}_{-0.019}$	0.991	$\pm 0.001^{+0.013}_{-0.022}$	1.139	$\pm 0.001^{+0.013}_{-0.028}$
-0.306	0.970	$\pm 0.001^{+0.013}_{-0.019}$	1.022	$\pm 0.001^{+0.013}_{-0.021}$	1.177	$\pm 0.001^{+0.013}_{-0.026}$
-0.153	1.021	$\pm 0.001^{+0.015}_{-0.019}$	1.085	$\pm 0.001^{+0.015}_{-0.019}$	1.267	$\pm 0.001^{+0.015}_{-0.022}$
-0.000	1.079	$\pm 0.001^{+0.014}_{-0.017}$	1.154	$\pm 0.001^{+0.014}_{-0.016}$	1.367	$\pm 0.002^{+0.014}_{-0.012}$
0.153	1.021	$\pm 0.001^{+0.014}_{-0.019}$	1.085	$\pm 0.001^{+0.014}_{-0.020}$	1.267	$\pm 0.001^{+0.014}_{-0.021}$
0.306	0.969	$\pm 0.001^{+0.013}_{-0.019}$	1.022	$\pm 0.001^{+0.013}_{-0.022}$	1.178	$\pm 0.001^{+0.013}_{-0.029}$
0.460	0.943	$\pm 0.001^{+0.013}_{-0.019}$	0.991	$\pm 0.001^{+0.013}_{-0.023}$	1.142	$\pm 0.001^{+0.013}_{-0.030}$
0.613	0.930	$\pm 0.001^{+0.012}_{-0.019}$	0.978	$\pm 0.001^{+0.012}_{-0.022}$	1.125	$\pm 0.001^{+0.012}_{-0.028}$
0.766	0.928	$\pm 0.001^{+0.012}_{-0.020}$	0.975	$\pm 0.001^{+0.012}_{-0.023}$	1.122	$\pm 0.001^{+0.012}_{-0.028}$
0.919	0.926	$\pm 0.001^{+0.012}_{-0.019}$	0.973	$\pm 0.001^{+0.012}_{-0.021}$	1.120	$\pm 0.001^{+0.012}_{-0.027}$
1.072	0.929	$\pm 0.001^{+0.012}_{-0.020}$	0.976	$\pm 0.001^{+0.012}_{-0.024}$	1.125	$\pm 0.001^{+0.012}_{-0.030}$
1.225	0.929	$\pm 0.001^{+0.012}_{-0.019}$	0.975	$\pm 0.001^{+0.012}_{-0.022}$	1.122	$\pm 0.001^{+0.012}_{-0.027}$
1.379	0.931	$\pm 0.001^{+0.012}_{-0.019}$	0.978	$\pm 0.001^{+0.012}_{-0.021}$	1.126	$\pm 0.001^{+0.012}_{-0.026}$
1.532	0.934	$\pm 0.001^{+0.012}_{-0.018}$	0.980	$\pm 0.001^{+0.012}_{-0.020}$	1.129	$\pm 0.001^{+0.012}_{-0.024}$
1.685	0.936	$\pm 0.001^{+0.012}_{-0.019}$	0.983	$\pm 0.001^{+0.012}_{-0.021}$	1.133	$\pm 0.001^{+0.012}_{-0.026}$
1.838	0.939	$\pm 0.001^{+0.012}_{-0.018}$	0.986	$\pm 0.001^{+0.012}_{-0.020}$	1.135	$\pm 0.001^{+0.012}_{-0.024}$
1.991	0.943	$\pm 0.001^{+0.012}_{-0.019}$	0.991	$\pm 0.001^{+0.012}_{-0.022}$	1.141	$\pm 0.001^{+0.012}_{-0.026}$
2.144	0.949	$\pm 0.001^{+0.013}_{-0.019}$	0.998	$\pm 0.001^{+0.013}_{-0.022}$	1.152	$\pm 0.001^{+0.013}_{-0.028}$
2.298	0.953	$\pm 0.001^{+0.013}_{-0.018}$	1.002	$\pm 0.001^{+0.013}_{-0.021}$	1.156	$\pm 0.001^{+0.013}_{-0.025}$
2.451	0.960	$\pm 0.001^{+0.013}_{-0.017}$	1.010	$\pm 0.001^{+0.013}_{-0.019}$	1.167	$\pm 0.001^{+0.013}_{-0.021}$
2.604	0.967	$\pm 0.001^{+0.013}_{-0.017}$	1.018	$\pm 0.001^{+0.013}_{-0.018}$	1.179	$\pm 0.001^{+0.013}_{-0.021}$
2.757	0.974	$\pm 0.001^{+0.013}_{-0.016}$	1.027	$\pm 0.001^{+0.013}_{-0.017}$	1.191	$\pm 0.001^{+0.013}_{-0.019}$
2.910	0.981	$\pm 0.001^{+0.013}_{-0.015}$	1.034	$\pm 0.001^{+0.013}_{-0.014}$	1.202	$\pm 0.001^{+0.013}_{-0.014}$
3.063	0.986	$\pm 0.001^{+0.013}_{-0.015}$	1.041	$\pm 0.001^{+0.013}_{-0.015}$	1.213	$\pm 0.001^{+0.013}_{-0.016}$

Table 3: The average transverse momenta of particles as a function of the distance between the leading particle and other particles in an event, see Fig. 25. The statistical and systematical uncertainties are given separately.

$\langle N \rangle$ vs $p_T(lead)$		
	Transverse region	
bin center	value	error
1.250	0.218	$\pm 0.000^{+0.024}_{-0.003}$
1.750	0.409	$\pm 0.001^{+0.017}_{-0.001}$
2.500	0.712	$\pm 0.001^{+0.018}_{-0.012}$
3.500	1.033	$\pm 0.002^{+0.036}_{-0.040}$
5.000	1.205	$\pm 0.002^{+0.065}_{-0.064}$
7.000	1.273	$\pm 0.004^{+0.096}_{-0.083}$
9.500	1.277	$\pm 0.007^{+0.112}_{-0.074}$
12.500	1.352	$\pm 0.016^{+0.108}_{-0.060}$
15.500	1.434	$\pm 0.030^{+0.089}_{-0.046}$
18.500	1.436	$\pm 0.045^{+0.106}_{-0.099}$
22.000	1.509	$\pm 0.063^{+0.065}_{-0.080}$
26.000	1.418	$\pm 0.090^{+0.173}_{-0.036}$
30.000	1.517	$\pm 0.137^{+0.213}_{-0.197}$

Table 4: The average number of particles per event in one unit interval in η and ϕ as a function of the $p_T(lead)$ for the transverse region, see Fig. 26. The statistical and systematical uncertainties are given separately.

$\langle p_T^{sum} \rangle$ GeV vs $p_T(lead)$		
	Transverse region	
bin center	value	error
1.250	1.681	$\pm 0.003^{+0.185}_{-0.024}$
1.750	3.528	$\pm 0.006^{+0.146}_{-0.015}$
2.500	6.881	$\pm 0.009^{+0.158}_{-0.144}$
3.500	10.855	$\pm 0.019^{+0.440}_{-0.525}$
5.000	13.302	$\pm 0.027^{+0.798}_{-0.835}$
7.000	14.481	$\pm 0.059^{+1.113}_{-1.080}$
9.500	14.910	$\pm 0.098^{+1.222}_{-1.012}$
12.500	16.199	$\pm 0.231^{+1.268}_{-0.837}$
15.500	17.764	$\pm 0.452^{+1.167}_{-0.643}$
18.500	18.247	$\pm 0.723^{+1.265}_{-1.412}$
22.000	19.056	$\pm 1.054^{+1.317}_{-1.641}$
26.000	16.882	$\pm 1.373^{+2.054}_{-0.266}$
30.000	21.053	$\pm 2.623^{+2.329}_{-3.342}$

Table 5: The average transverse momenta of particles as a function of the $p_T(lead)$ for the transverse region, see Fig. 28. The statistical and systematical uncertainties are given separately.

$\langle p_T \rangle$ [GeV] vs N						
bin center	Forward		Transverse		Away	
	value	error	value	error	value	error
3.000	1.021	$\pm 0.001^{+0.026}_{-0.012}$	0.769	$\pm 0.000^{+0.026}_{-0.004}$	0.759	$\pm 0.000^{+0.026}_{-0.008}$
7.500	1.076	$\pm 0.000^{+0.011}_{-0.012}$	0.886	$\pm 0.000^{+0.011}_{-0.006}$	0.865	$\pm 0.000^{+0.011}_{-0.007}$
12.500	1.119	$\pm 0.001^{+0.013}_{-0.016}$	0.959	$\pm 0.000^{+0.013}_{-0.011}$	0.939	$\pm 0.000^{+0.013}_{-0.014}$
17.500	1.151	$\pm 0.001^{+0.012}_{-0.023}$	1.011	$\pm 0.001^{+0.012}_{-0.018}$	0.992	$\pm 0.001^{+0.012}_{-0.021}$
22.500	1.180	$\pm 0.001^{+0.012}_{-0.035}$	1.053	$\pm 0.001^{+0.012}_{-0.032}$	1.034	$\pm 0.001^{+0.012}_{-0.030}$
27.500	1.201	$\pm 0.002^{+0.012}_{-0.043}$	1.087	$\pm 0.001^{+0.012}_{-0.037}$	1.072	$\pm 0.001^{+0.012}_{-0.039}$
32.500	1.230	$\pm 0.004^{+0.011}_{-0.055}$	1.118	$\pm 0.002^{+0.011}_{-0.053}$	1.102	$\pm 0.002^{+0.011}_{-0.045}$
37.500	1.241	$\pm 0.006^{+0.017}_{-0.065}$	1.141	$\pm 0.004^{+0.017}_{-0.046}$	1.129	$\pm 0.004^{+0.017}_{-0.052}$

Table 6: The average transverse momenta of particles as a function of particle multiplicity for different regions, see Fig. 30. The statistical and systematical uncertainties are given separately.